https://doi.org/10.5194/egusphere-2025-646
Preprint. Discussion started: 25 March 2025
© Author(s) 2025. CC BY 4.0 License.

Seismic Acquisition, Modelling, and Data Analysis of Antarctic subglacial lakes

Kai Lu[1] and Yuqing Chen[2]

[1]Key Laboratory of Polar Science, Polar Research Institute of China
[2]Key Laboratory of Intraplate Volcanoes and Earthquakes, China University of Geosciences (Beijing)

Correspondence: Yuqing Chen (yuqing_geo@cugb.edu.cn)

Abstract. Subglacial lakes are crucial for studying life evolution, ice sheet dynamics, and climate change. Lake Qilin, located in the Princess Elizabeth Land region of East Antarctica, is the second largest subglacial lake discovered in Antarctica. Studying its microbial communities and biogeochemical cycles provides valuable insights into Earth's life evolution and the search for extraterrestrial life. To advance this research, China plans to conduct clean drilling and water sampling in Lake Qilin from 2025 to 2027. Additionally, during the 41th Chinese National Antarctica Research Expedition, active-source seismic exploration will be conducted to obtain high-resolution imaging, guiding drilling site selection. This study provides theoretical support for these efforts by developing a representative velocity model for subglacial lakes, simulating wavefields to characterize seismic responses, processing simulated data to identify processing challenges, and evaluating acquisition systems to determine the optimal survey geometry for Lake Qilin exploration. The results demonstrate that, in addition to primary reflections, multiples and guided waves will prominently develop in the seismic wavefield. Conventional seismic data processing of multiples introduce false coherent events, complicating seismic interpretation. Furthermore, the full-coverage acquisition system is identified as the optimal approach for the Lake Qilin exploration. To validate our simulation results, seismic data from Thwaites Glacier were processed and analyzed, and the results aligning well with part of our simulations, thus confirming the accuracy of the theoretical framework.

1 Introduction

To date, more than 670 subglacial lakes have been identified beneath the Antarctic ice sheet. These lakes sit under ice layers of several kilometers thick and exist in extreme conditions—high pressure, freezing temperatures, complete darkness, and nutrient-scarce environments (Siegert, 2018; Livingstone et al., 2022). They resemble early Earth conditions and even those found on other celestial bodies. Studying the microbial communities in these lakes and their role in biogeochemical cycles can offer critical insights into the evolution of life on Earth (Christner et al., 2014; Mikucki et al., 2016) and the search for extraterrestrial life (Garcia-Lopez and Cid, 2017). Meanwhile, the sediment at the bottom of these lakes likely records geological and climatic changes before the overlying ice sheet even formed, serving as important archives for studying the evolution of the Antarctic ice sheet and global climate change (Filina et al., 2007; Bentley et al., 2011; Smith et al., 2018; Yan et al., 2022; Siegfried et al., 2023). In addition, active subglacial lakes (Siegfried and Fricker, 2018), which are connected to vast networks of subglacial water systems (Wingham et al., 2006), can reduce the shear stress at the base of the ice sheet, speeding up ice movement and influencing the stability and mass balance of the ice sheet (Stearns et al., 2008; Horgan et al., 2012; Li et al., 2021). Furthermore, these lakes deliver massive amounts of freshwater and nutrients to the Southern Ocean (Livingstone et al., 2013; Pattyn et al., 2016; Vick-Majors et al., 2020), playing a key role in its ecosystem.

The West Antarctic Ice Sheet (WAIS) rests on the seafloor, making it particularly sensitive to climate change due to its inherent instability mechanisms (Joughin and Alley, 2011). Ice sheet modeling results indicate that during the deglaciation period tens of thousands of years ago, the overlying ice sheet above the Whillans and Mercer subglacial lakes completely melted and was replaced by seawater. Integration of remote observations and numerical modelling reveal that these hydrologically active subglacial lakes have drainage and recharge cycles lasting from several months to several years (Winberry et al., 2009; Siegert et al., 2016). Water flows between lakes via subglacial channels before eventually discharging into the surrounding ocean (Napoleoni et al., 2020). In contrast, the East Antarctic Ice Sheet (EAIS) rests predominantly on bedrock well above sea level(Cui et al., 2020b; Glaciers, 2024). Ice sheet modeling results suggest that the EAIS began to form approximately 34 million years ago and reached its current extent around 14 million years ago, remaining relatively stable since then without significant changes (Contributors, 2024). As a result, subglacial lakes in East Antarctica have preserved critical records of Earth's climate history and the evolution of the Antarctic ice sheet, offering invaluable insights into these processes (Jamieson et al., 2023).

Since 2015, China has conducted over 150,000 kilometers of airborne geophysical surveys in the Princess Elizabeth Land region of East Antarctica, utilizing the "Snow Eagle 601" fixed-wing aircraft equipped with advanced ice-penetrating radar, gravimeters, and magnetometers (Cui et al., 2018, 2020a). Through comprehensive analysis and processing of airborne geophysical data, researchers identified a large subglacial lake located more than 3,000 meters beneath the ice sheet, which was subsequently named "Lake Qilin." Satellite altimetry data further indicated that the lake exhibits relatively stable hydrological characteristics, with no significant evidence of water discharge or recharge events (Yan et al., 2022). Therefore, Lake Qilin offers significant research opportunities for studying life processes in extreme environments, climate change, and the evolution of the Antarctic ice sheet. During the 40th Chinese Antarctic Research Expedition, the research team successfully established access routes to the lake. In the upcoming 41st Chinese Antarctic Research Expedition, active-source seismic surveys are scheduled to be carried out over Lake Qilin. These surveys utilize high-resolution seismic imaging to characterize the lake's internal structure and the overlying ice sheet, providing essential data for optimizing future drilling site selection.

To support seismic exploration at Lake Qilin and extend its applicability to other subglacial lake studies, this study develops a representative velocity model and conducts a systematic analysis of wavefield simulation, seismic data processing, and observation system evaluation. Initially, Wavefield simulations were conducted to investigate the impact of polar geological structures, such as subglacial lakes and firn layers, on seismic wavefield characteristics. Following this, synthetic seismic data derived from the subglacial lake model were analyzed to identify key challenges in seismic data processing and propose potential solutions. Furthermore, a thorough evaluation of three seismic observation systems was carried out to determine the most suitable approach for seismic exploration at Lake Qilin. To conclude, seismic data from Thwaites Glacier were processed and analyzed, validating the accuracy of the proposed theoretical framework.

© Author(s) 2025. CC BY 4.0 License.

2 Seismic Wavefield modeling of Subglacial Model

Figure 1 illustrates a typical subglacial velocity model, with a depth of 3.6 km and a horizontal extent of 10 km. The model consists of a thick ice sheet, a subglacial lake, and the underlying bedrock. The ice sheet is 2400 meters thick, with a velocity of 3800 m/s Yan et al. (2020). Although ice layers are typically stratified, the negligible impedance contrasts between them allow the ice sheet to be approximated as a homogeneous isotropic medium. The subglacial lake is 500 meters deep, with a velocity of 1500 m/s. For simplification, the lake bed is assumed to be flat in the center and sloping at the edges. The bedrock beneath the lake has a velocity of 5200 m/s (Maguire et al., 2021). Building upon this model, we systematically investigate the seismic wavefield propagation characteristics under various conditions, including absorbing boundaries, firn layers, the free surface, and sediment layers. The wavefield simulation is performed using a first-order acoustic wave equation within a staggered-grid finite-difference framework (Chen et al., 2020). Both the source and receivers are placed on the surface of the ice sheet, with receivers evenly spaced at 5-meter intervals across the entire surface. A Ricker wavelet with a central frequency of 20 Hz is employed as the source, with a time sampling interval of 0.5 ms and a total simulation time of 5 seconds.

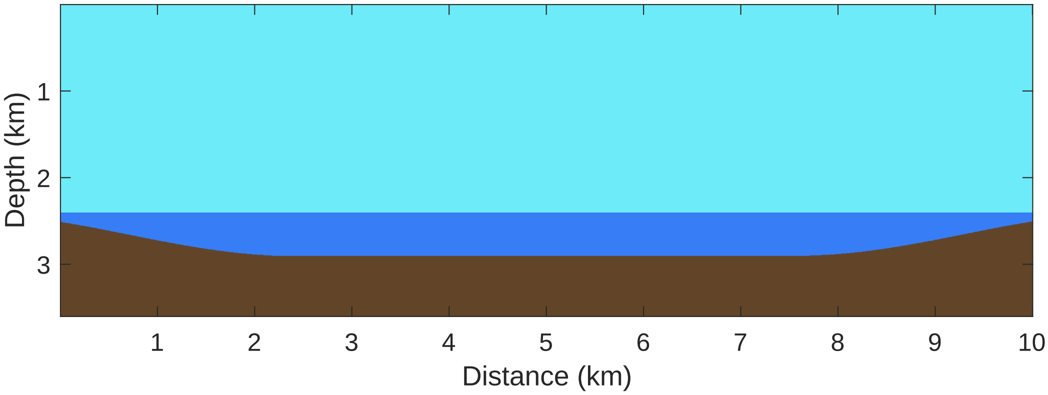

Figure 1. A typical subglacial velocity model with an ice sheet, a subglacial lake and bedrock.

2.1 Absorbing boundary

When the model is surrounded by absorbing boundaries, seismic waves do not reflect upon reaching the model's edges. Consequently, wave propagation is primarily influenced by the subglacial geological structure and its elastic properties (velocity and density). The substantial impedance contrast between the ice sheet, subglacial lake, and bedrock leads to strong reflections at the ice-water and water-bedrock interfaces.

Figure 2 presents wavefield snapshots at various time steps. Upon triggering the source (indicated by a red pentagram), a direct wave (Figure 2a) is generated and propagates downward as a spherical wave. Upon reaching the ice-water interface (Interface 1), part of the energy is reflected, forming the primary reflection wave R_1 (Figure 2b). Due to the significant impedance contrast between ice and water, the reflection coefficient at the ice-water interface is negative, resulting in a polarity reversal

of the reflected wave. Additionally, a portion of the direct wave's energy transmits downward into the lake. When this energy reaches the water-bedrock interface (Interface 2), it generates the primary reflection wave R_2 at the water-bedrock boundary (Figures 2c and 2d). The reflected wave R_2 then propagates upward and partially reflects downward again at the ice-water interface, returning to the lake. This wave reflects once more at the ice-water boundary, forming a first-order interlayer multiple
85 $R_2R_1R_2$ (Figures 2e and 2f). This interlayer multiple continues to oscillate within the water layer, generating higher-order multiples.

Figure 11 illustrates the seismic records obtained from surface-deployed geophones, with various orders of interlayer multiples appearing at regular time intervals. These intervals are primarily influenced by the thickness of the water layer. Moreover, the seismic records exhibit a distinct "zigzag" pattern (highlighted by red boxes in Figure 11a), which is attributed to the
90 concave geometry of the lake boundary.

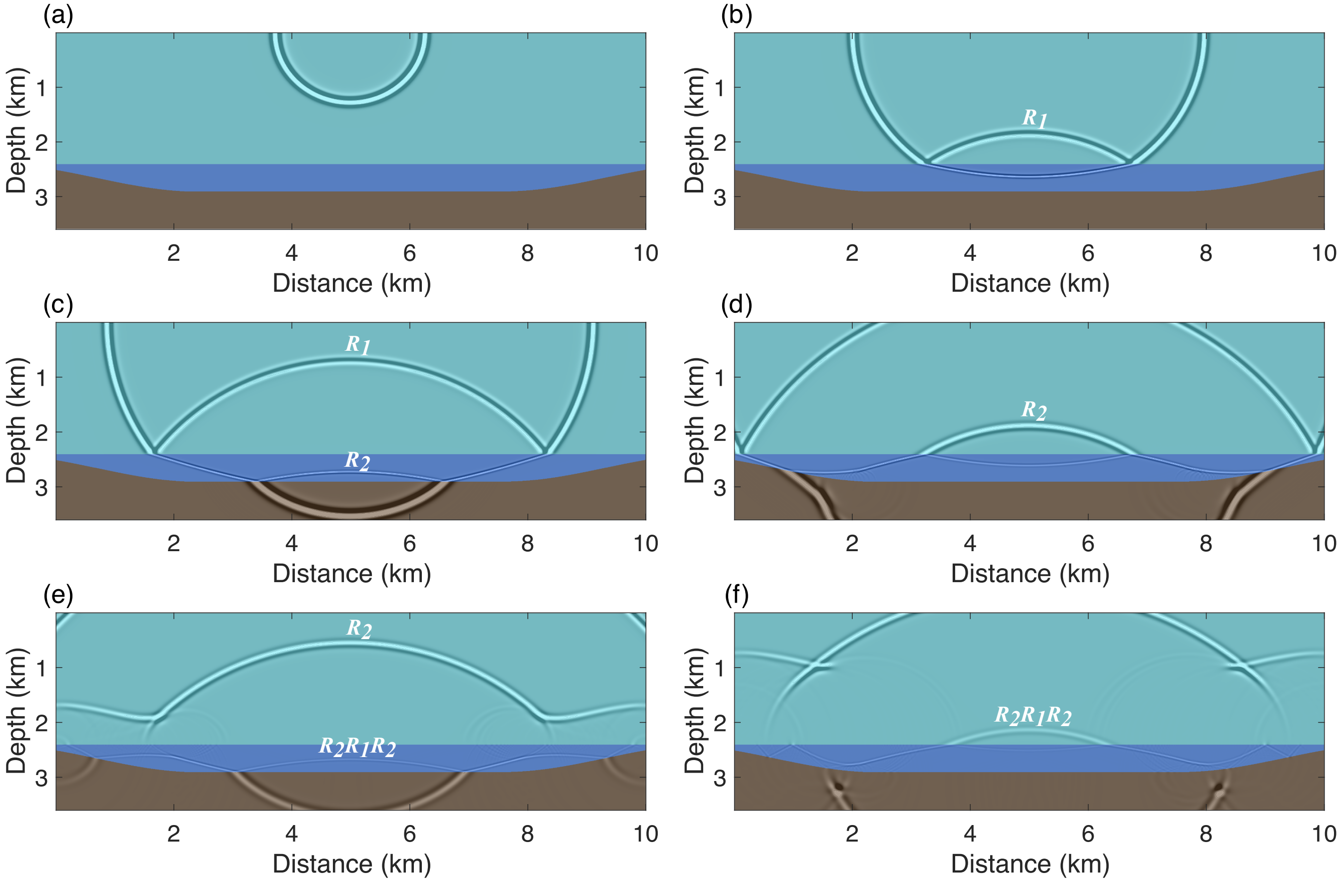

Figure 2. The wavefield snapshots at different time steps when the model is surrounded by absorbing boundaries, where (a) to (f) represent the wavefield snapshots at $t = 0.4$s, $t = 0.85$s, $t = 1.15$s, $t = 1.5$s, $t = 1.85$s, and $t = 2.1$s, respectively.

https://doi.org/10.5194/egusphere-2025-646
Preprint. Discussion started: 25 March 2025
© Author(s) 2025. CC BY 4.0 License.

2.2 Free surface

The ice sheet surface serves as a distinct boundary where the elastic properties of the overlying air, including velocity and density, are negligible relative to those of the ice. Consequently, the air-ice interface satisfies the zero-stress condition, commonly referred to as the free surface boundary condition (Lan and Zhang, 2011). In this model, the ice sheet surface is treated as a free surface to investigate the effect of this boundary condition on seismic wave propagation.

As illustrated in Figure 3a, before the primary reflections R_1 and R_2 reach the surface, seismic wave propagation follows the pattern observed under absorbing boundary conditions (Figure 2c). Upon reaching the surface, the primary reflection R_1 is fully reflected with reversed polarity (denoted as R_1F) in Figures 3b and 3c, due to the free surface acting as a boundary with a reflection coefficient of -1. When the downward reflection R_1F encounters the ice-water interface again, part of its energy is reflected upward, generating the first-order free surface multiple R_1FR_1, as shown in Figure 3d. This wave continues to reflect between the free surface and the ice-water interface, generating the 2nd order free surface multiple $R_1FR_1FR_1$ in Figure 3f, and higher-order multiples. Similarly, the primary reflection R_2 also generates 1st order R_2FR_2 (Figure 3e) and higher order free surface multiples by reflecting between these two interfaces.

In addition, the first-order interlayer multiple $R_2R_1R_2$ (depicted by the blue dashed line in Figure 3d), which follows R_1F, also reflects repeatedly within the ice sheet, generating hybrid multiples that involve both the water layer and the free surface. The reflected wave, indicated by the green dashed line in Figure 3e, results from the superposition of the first-order free surface multiples R_2FR_1 and R_1FR_2, which originate from the ice-water and water-bedrock interfaces. Figures 4a and 4b illustrate the ray paths of R_2FR_1 and R_1FR_2 (simplified as straight lines). Since both waves share the same propagation direction, velocity, arrival time, and polarity, their constructive interference amplifies the reflected wave.

Figure 11b presents seismic records under free surface boundary conditions. In addition to the primary reflections and multiples seen in Figure 10a, it includes free surface multiples. The seismic event of the first and second order free surface multiple, R_1FR_1 and $R_1FR_1FR_1$, have similar curvatures and appear at regular intervals determined by the ice thickness. Additionally, the superposition of R_2FR_1 and R_1FR_2 shows increased amplitude, and its time difference from the primary reflection R_2 also depends on the ice thickness

2.3 Firn layer

Firn is a porous, transitional layer in polar ice sheets, located between freshly fallen snow and glacial ice (Hollmann et al., 2021). It covers about 99% of the Antarctic ice sheet and roughly 90% of the Greenland ice sheet, playing a vital role in understanding ice-sheet mass balance, hydrology, and paleoclimate (Diez et al., 2013; Schlegel et al., 2019; fir, 2024). The thickness of the firn layer ranges from a few meters to over 100 meters across the ice sheets of Greenland and Antarctica. Its density increases with depth due to the densification and metamorphosis of snow into glacial ice (Zhou et al., 2022; Pearce et al., 2022; Chaput et al., 2022). To assess the impact of the firn layer on wavefield propagation, we added a 125-meter-thick firn layer to the top of the ice sheet in our model (Figure 5a), where the velocity increases from 1400 m/s to 3850 m/s, transitioning smoothly at the firn-ice interface (Figure 5b).

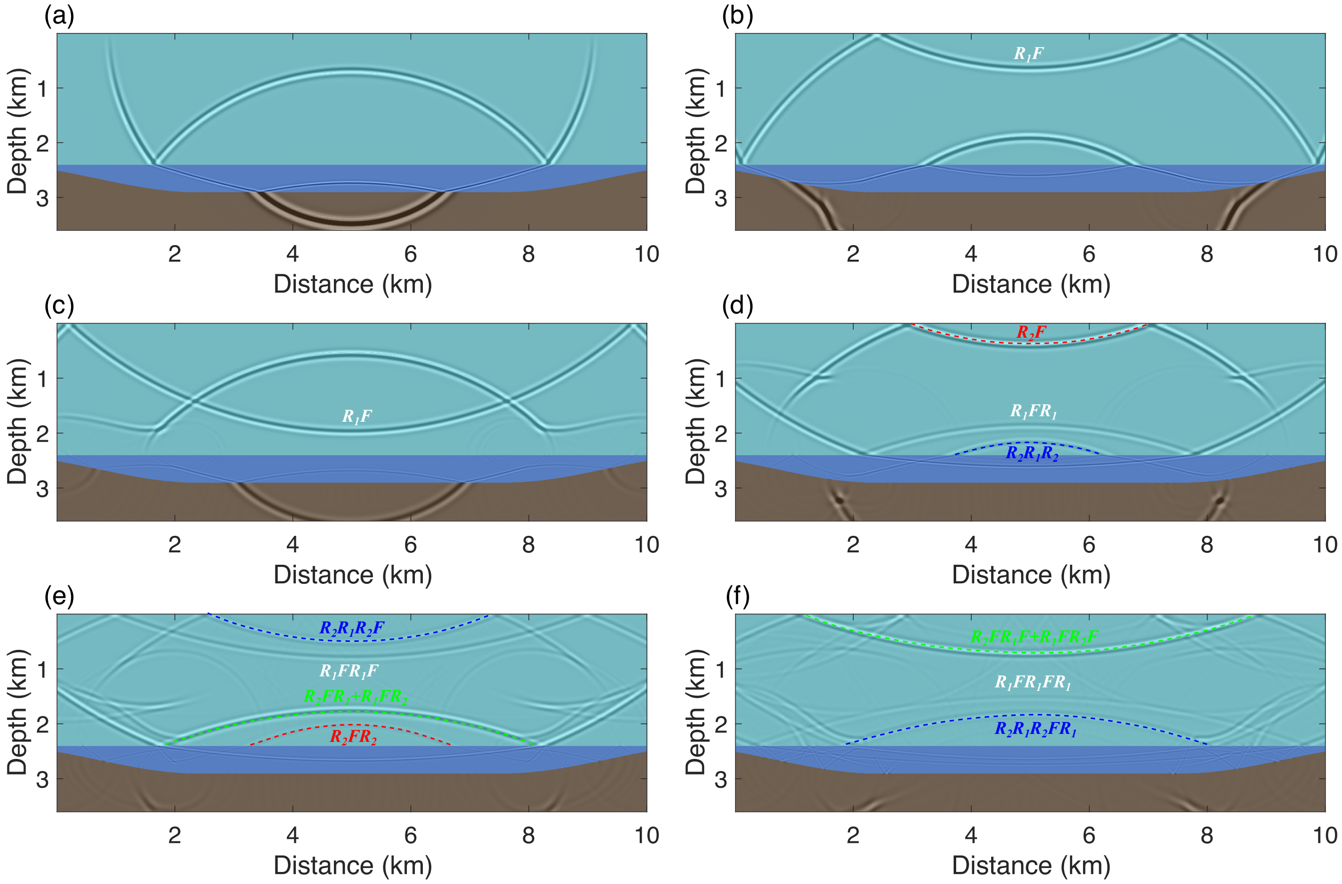

Figure 3. The wavefield snapshots at different time steps when the free surface is added to the top of the model, where (a) to (f) represent the wavefield snapshots at $t = 1.15$s, $t = 1.5$s, $t = 1.85$s, $t = 2.1$s, $t = 2.8$s, and $t = 3.45$s, respectively.

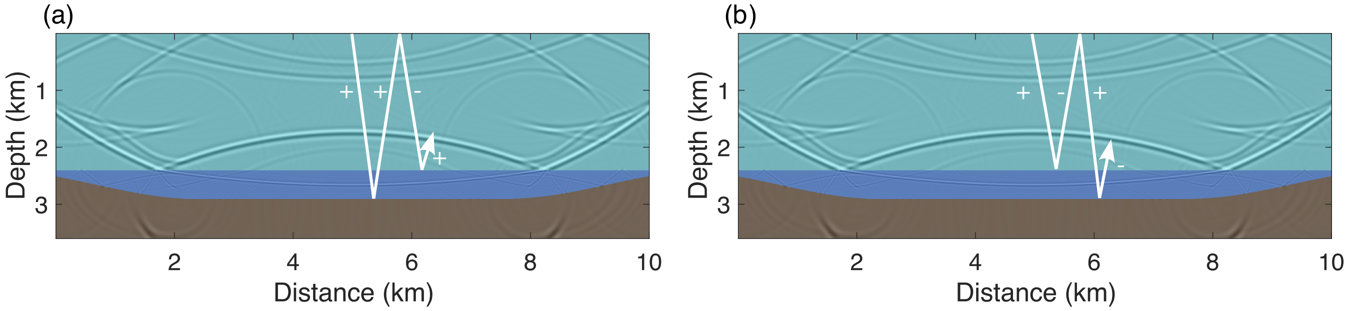

Figure 4. Demonstration of ray paths of free surface multiple R_2FR_1 and R_1FR_2.

Due to the significant velocity gradient within the firn layer, refracted waves emerge at relatively short offsets (indicated by the white arrow in Figure 6) and propagate at the velocity of the underlying glacial ice. In contrast, the direct wave, within the red box in Figure 6, travels more slowly along the surface at the velocity of the upper firn layer. This feature is more clearly illustrated in Figure 7, which provides a zoomed-in view of the wavefield within the top 250 m. As a result, in seismic records, the first arrivals are primarily refracted waves, while the direct wave appears as a straight line with a steep slope (shown by the red dashed line in Figure 11c). Additionally, the firn-ice interface (F_s) behaves similarly to a free surface, exhibiting a negative reflection coefficient when waves are incident from the ice layer. Consequently, the upgoing primary reflections R_1 and R_2 generate downgoing reflected waves R_1F_s and R_2F_s with reversed polarity (Figures 6d and 6e). Subsequent multiple reflections follow this pattern. However, due to the smaller reflection coefficient of the firn-ice interface, the energy of these reflected waves diminishes rapidly with successive reflections, as shown in Figure 11c.

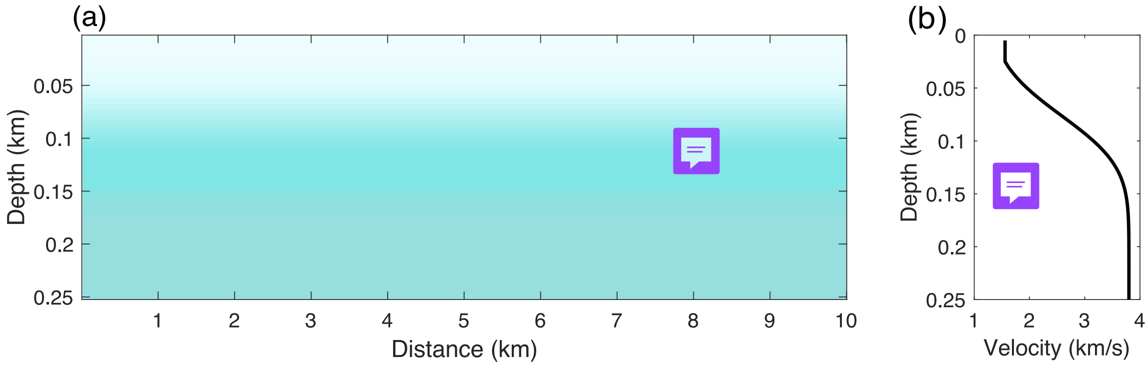

Figure 5. A zoomed-in view of the subglacial model showing the firn layer in the top 125 meters, (b) the 1D vertical profile of the model shown in (a).

2.4 Firn layer and free surface

In real-world scenarios, the firn layer and the free surface may coexist. To account for this, both are incorporated into our wavefield simulations. As illustrated in Figure 8, a key feature is the generation of free surface multiples of various orders within the firn layer, including both reflection and refraction waves. Due to the thinness of the firn layer, first-order free surface multiples (R_sF) are generated almost immediately. As propagation continues, higher-order multiples, such as second-order R_sFR_sF (white arrow in Figure 8c), third-order $R_sFR_sFR_sF$ (white arrow in Figure 8d), and even higher-order multiples, are rapidly formed. However, as the order increases, the energy of these multiples diminishes quickly due to the small reflection coefficient of the firn-ice interface.

Multiple orders of refracted waves also propagate within the firn layer, with their wavepaths shown in Figure 9. Higher-order refracted waves emerge later in time and require longer offsets to be observed. Due to the rapid increase in the reflection coefficient at the firn-ice interface near the critical angle, the energy of these refracted waves remains relatively constant as their order increases. In seismic records (Figure 11), these refracted waves are represented as a series of linear events with

https://doi.org/10.5194/egusphere-2025-646
Preprint. Discussion started: 25 March 2025
© Author(s) 2025. CC BY 4.0 License.

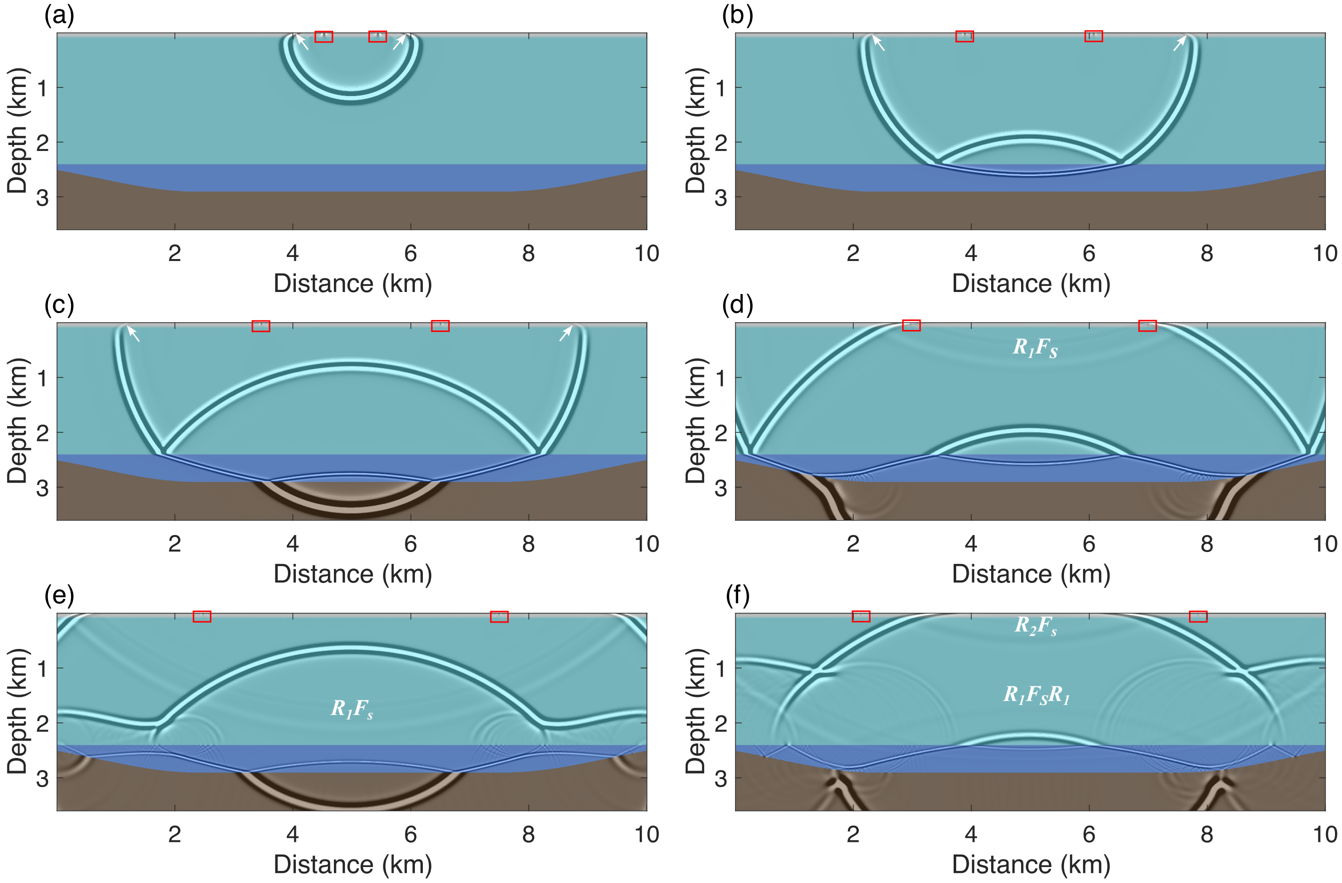

Figure 6. The wavefield snapshots at different time steps when a firn layer is incorporated into the subglacial model, where (a) to (f) represent the wavefield snapshots at $t = 0.4$s, $t = 0.85$s, $t = 1.15$s, $t = 1.5$s, $t = 1.85$s, and $t = 2.1$s, respectively.

identical slopes, consistent time delays, and uniform offset intervals, commonly referred to as guided waves. Analyzing these guided waves provides valuable insights into the structure of the firn layer (Boiero et al., 2013; Li et al., 2018).

2.5 Sediment layer

Sediment in subglacial lakes often contains paleoenvironmental records, such as those related to ice sheet history and climate change. These records are crucial for understanding past climate patterns, ice sheet dynamics, and geological history, all of which have significant scientific implications. To evaluate the impact of the sediment layer on seismic wave propagation, we incorporated a 200-meter-thick sediment layer, with a velocity of 3750 m/s (Peters et al., 2008; Maguire et al., 2021), at the base of the subglacial lake (Anandakrishnan and Winberry, 2004), while excluding the effects of the firn layer and free surface in our simulations.

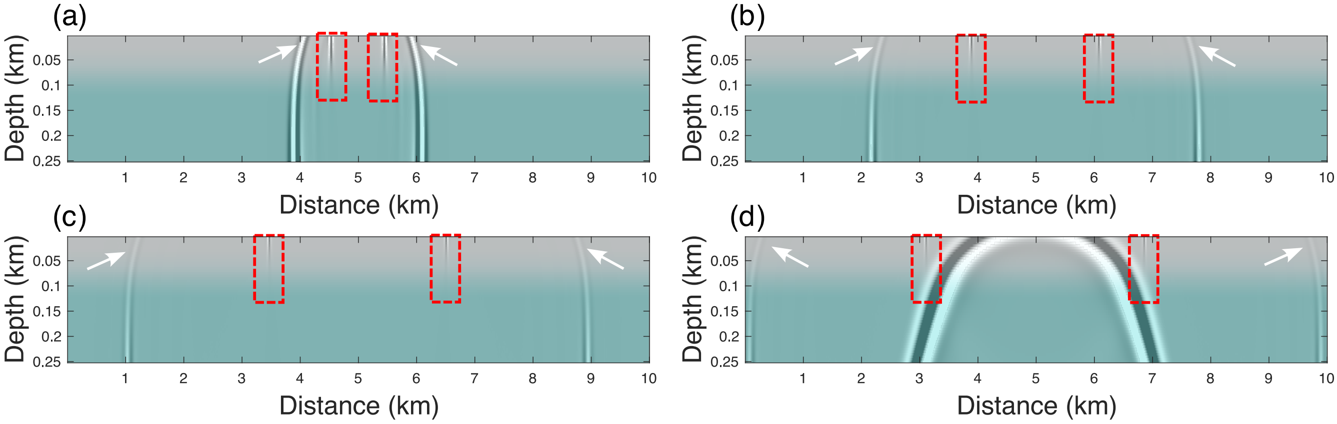

Figure 7. A zoomed-in view of the wavefield snapshots in the firn layer at $t = 0.4$s, $t = 0.85$s, $t = 1.15$s and $t = 1.4$s.

The presence of a sediment layer introduces a significant feature: the generation of interlayer multiples within the sediment. As shown in Figure 10a, the downgoing direct wave initially generates primary reflections R_1, R_2, and R_3 at the ice-water, water-sediment, and sediment-bedrock interfaces, respectively. Due to the thinness of the sediment layer, reflection R_3 quickly produces a first-order interlayer multiple, $R_3R_2R_3$, within the sediment shown in Figure 10c. This interlayer multiple continues to oscillate within the sediment, generating higher-order multiples. Furthermore, reflections R_2 and R_3 oscillate within the water layer, forming a first-order interlayer multiple, $R_2R_1R_2$, within the water layer (Figure 10e), and $R_3R_1R_2$ across both the sediment and water layers (Figure 10e).

In the seismic records shown in Figure 11e, reflections R_2 and R_3, along with the first-order interlayer multiples $R_2R_1R_2$ and $R_3R_1R_2$, as well as higher-order interlayer multiples, consistently appear in pairs. The time lag between seismic events within each pair is primarily influenced by the sediment layer thickness, while the time difference between pairs is governed by the water layer thickness. Furthermore, due to the low reflection coefficient at the sediment-bedrock interface, the amplitude of interlayer multiples within the sediment rapidly decreases with increasing order. In contrast, the amplitude of interlayer multiples within the water layer diminishes more gradually, due to the higher reflection coefficients at the ice-water and water-sediment interfaces.

3 Seismic data processing

Prestack seismic data collected in the field do not directly reveal subglacial geological structures. To accurately determine subglacial properties and structures, data processing techniques such as denoising, static correction, velocity analysis, dynamic correction, stacking, and migration are necessary (Yilmaz, 2001). Using the five geological models discussed earlier, we will conduct multi-shot simulations and generate the corresponding stacked images, which will be used to analyze the subglacial wavefield and geological structures.

https://doi.org/10.5194/egusphere-2025-646
Preprint. Discussion started: 25 March 2025
© Author(s) 2025. CC BY 4.0 License.

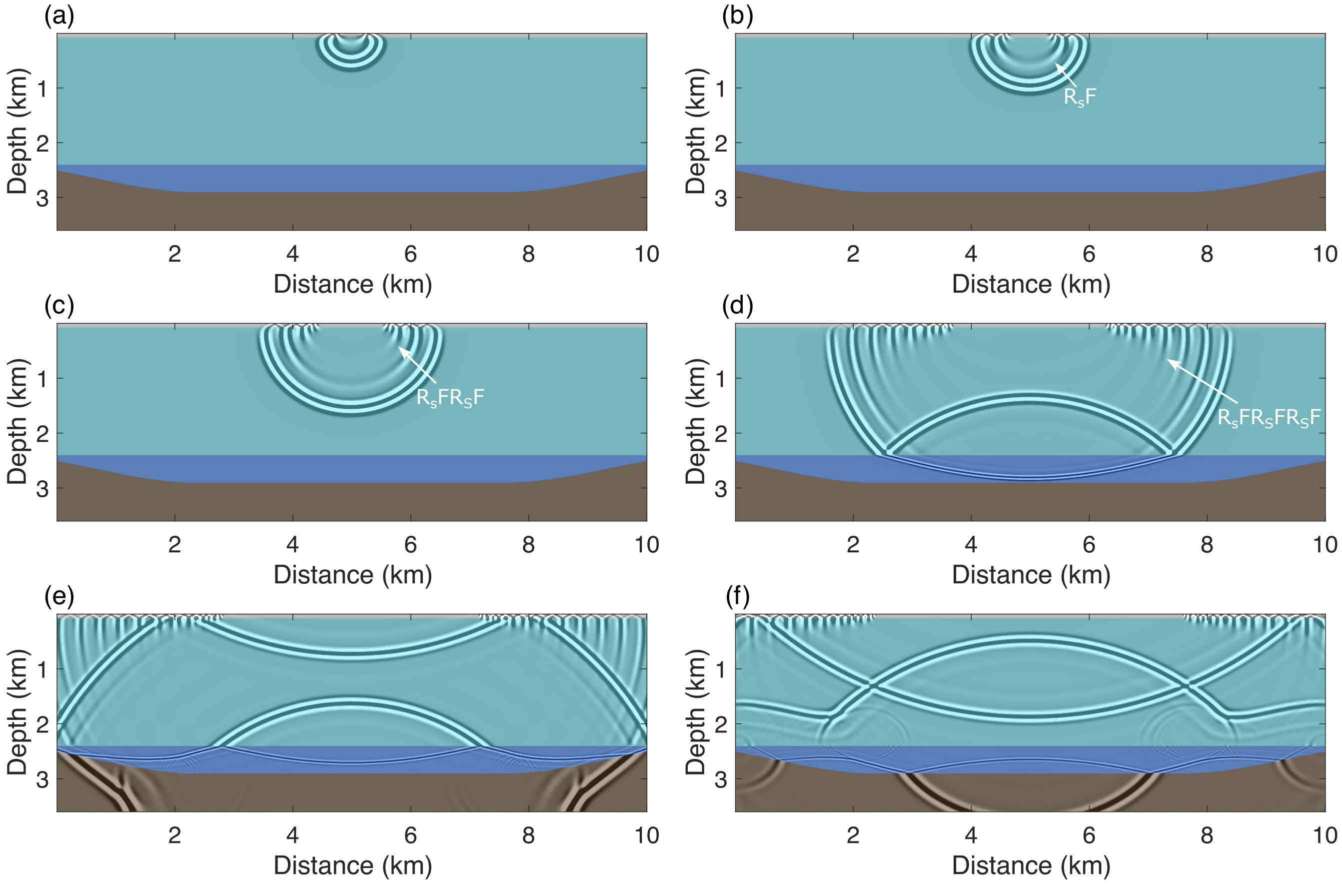

Figure 8. The wavefield snapshots at different time steps when both firn layer and free surface are incorporated into the subglacial model, where (a) to (f) represent the wavefield snapshots at $t = 0.235$s, $t = 0.35$s, $t = 0.5$s, $t = 1.0$s, $t = 1.6$s, and $t = 1.9$s, respectively.

3.1 Velocity analysis

We perform 100-shot simulations, with shot points spaced 100 meters apart across the ice sheet surface. Each shot gather contains 500 traces, with a receiver spacing of 20 meters. Since the simulated data are noise-free and the model surface is flat, no denoising or static correction is required during processing. Following the velocity analysis procedure, we first convert the common shot gathers (CSG) into common midpoint gathers (CMP), then compute the velocity spectrum (Yilmaz, 2001). Figure 12 presents the velocity spectra for the CMP gathers at $x = 5$ km of the five models. The horizontal axis represents stacking velocity, while the vertical axis represents two-way travel time. The energy clusters in the velocity spectra is computed by stacking reflection events along hyperbolic trajectories defined by the stacking velocity in the CMP gathers (Luo and Hale, 2012).

https://doi.org/10.5194/egusphere-2025-646
Preprint. Discussion started: 25 March 2025
© Author(s) 2025. CC BY 4.0 License.

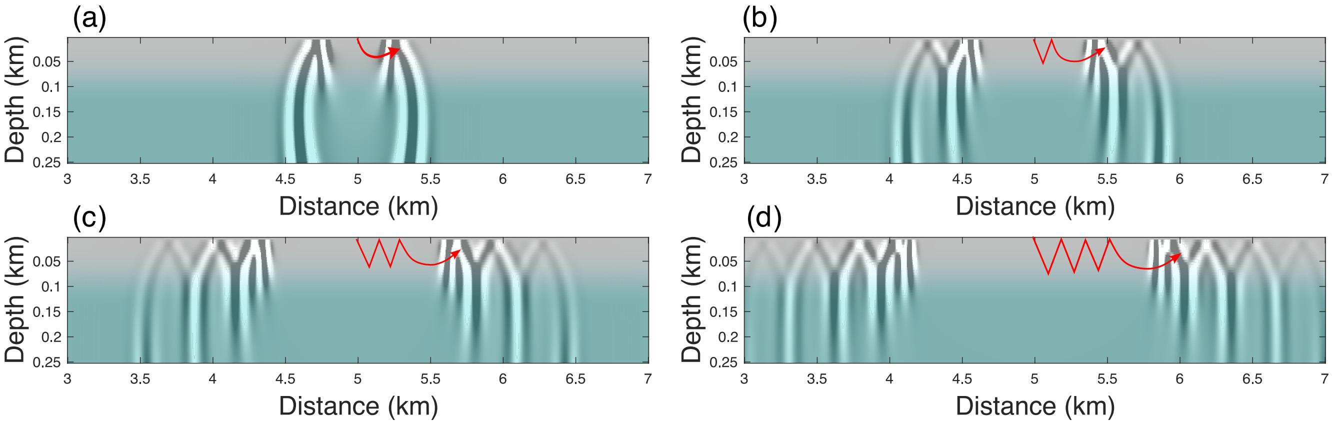

Figure 9. A zoomed-in view of the wavefield snapshots in the firn layer at $t = 0.235$s, $t = 0.35$s, $t = 0.5$s and $t = 1.0$s.

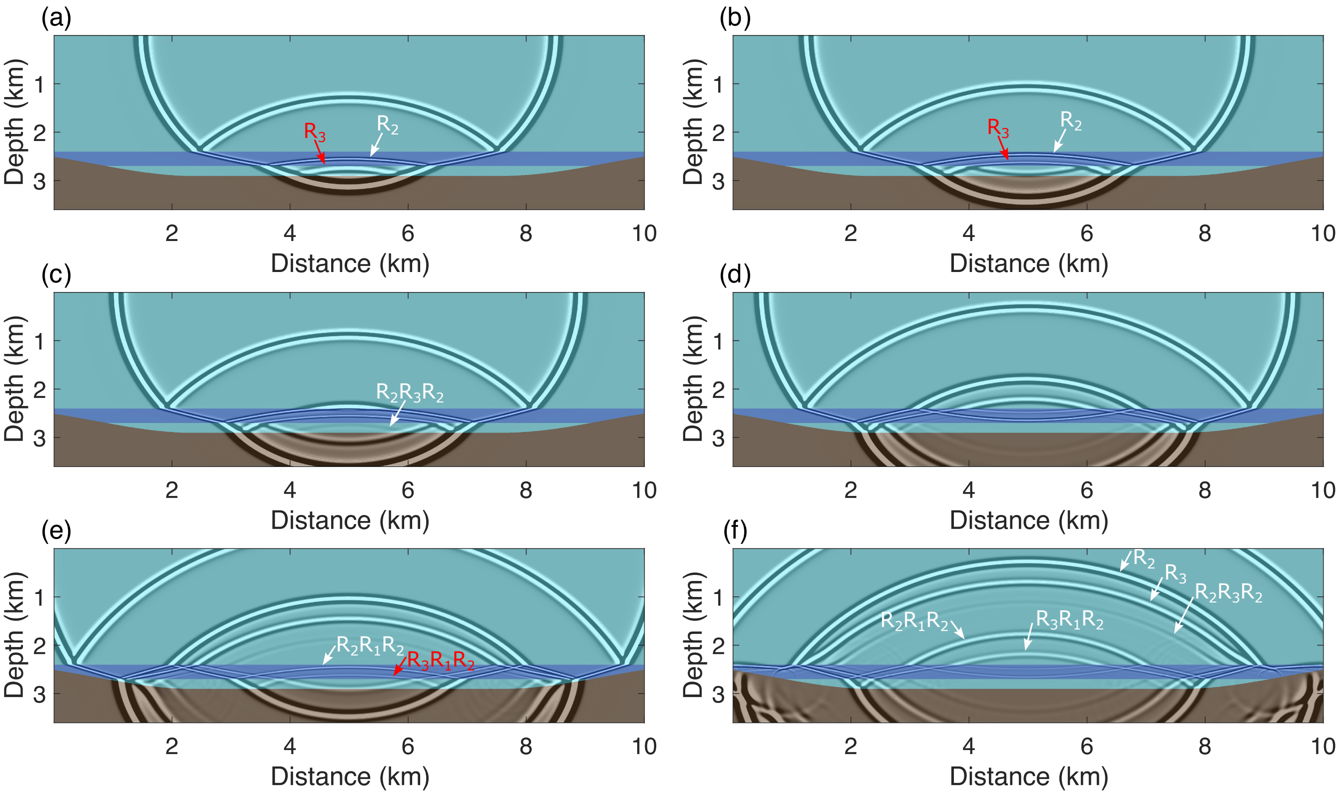

Figure 10. The wavefield snapshots at different time steps when a sediment layer is added at the bottom of the subglacial model, with (a) to (f) representing the wavefield snapshots at $t = 0.99$s, $t = 1.05$s, $t = 1.1$s, $t = 1.25$s, $t = 1.45$s, and $t = 1.65$s, respectively.

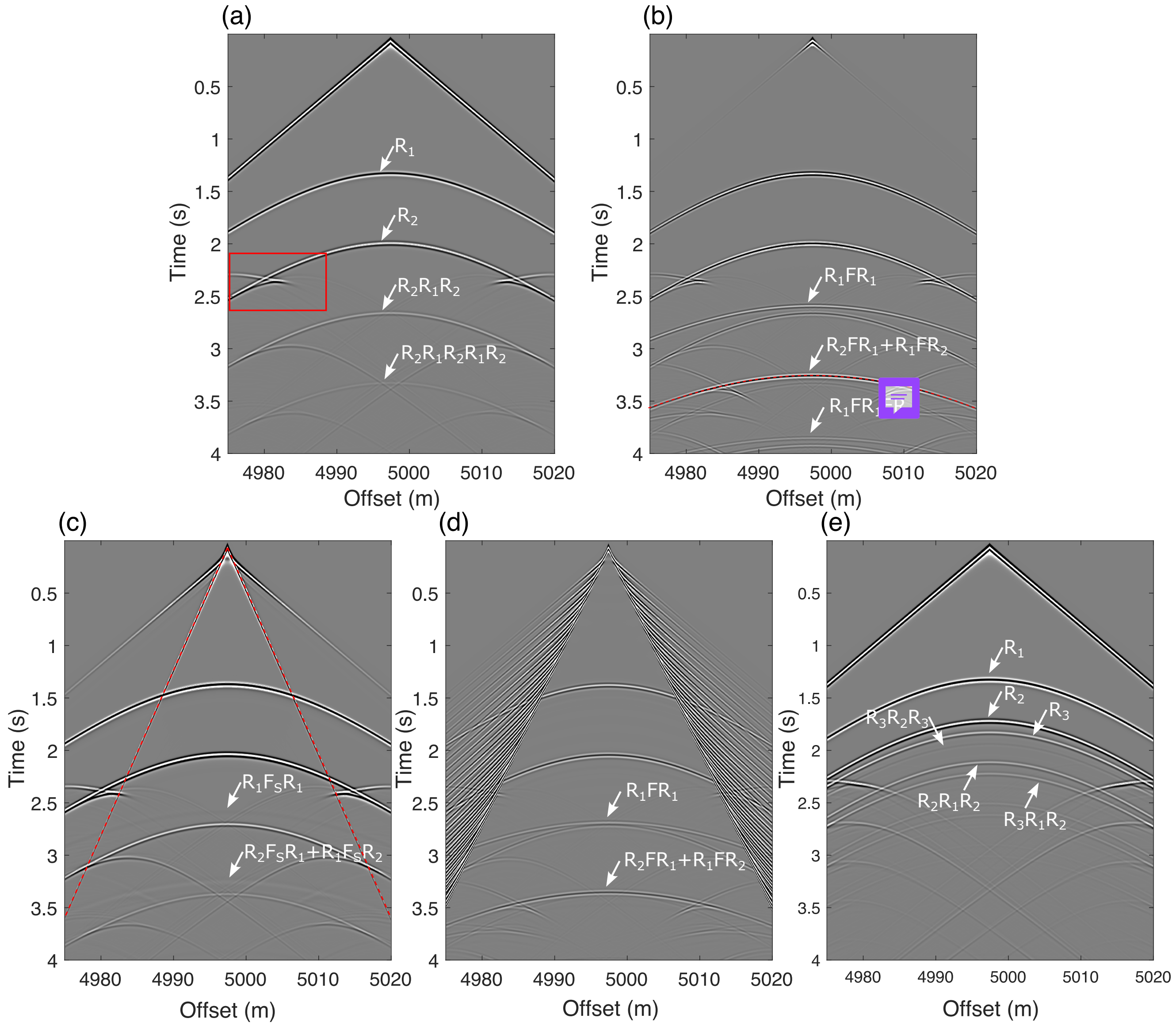

Figure 11. A common shot gather generated by the subglacial model, with (a) absorbing boundary, (b) free surface, (c) firn layer, (d) free surface + firn layer, and (e) sediment layer.

The energy clusters in Figure 12a represent, from top to bottom, the primary reflections R_1 and R_2 at the ice-water and water-bedrock interfaces, respectively, as well as the first-order interlayer multiple $R_2R_1R_2$ in the water layer. Due to the significantly lower velocity of water compared to glacial ice, the stacking velocity of R_2 is lower than that of R_1. Furthermore, as $R_2R_1R_2$ travels further within the water layer and is treated as a primary reflection during velocity analysis, its stacking velocity is also lower than that of R_2. Higher-order multiples within the water layer exhibit even lower stacking velocities, but these energy clusters are challenging to detect due to rapid amplitude attenuation after multiple reflections.

When the free surface is included in the model, the velocity spectrum not only retains the energy clusters seen in Figure 12a (highlighted by the red dash box) but also reveals strong energy clusters associated with free surface multiples. The stacking velocities of the first-order (R_1FR_1) and second-order ($R_1FR_1FR_1$) free surface multiples at the ice-water interface are close to that of the primary reflection R_1, while the first-order interlayer multiples R_2FR_1 and R_1FR_2 exhibit relatively lower stacking velocities.

When a firn layer is included in the model, the firn-ice interface produces effects similar to a free surface. However, due to the low reflection coefficient at the firn-ice interface, the corresponding multiples $R_1F_sR_1$, $R_2F_sR_1$, and $R_1F_sR_2$ are difficult to distinguish in Figure 12c. Guided waves appear in the seismic data when both the firn layer and free surface are present. However, since the guided waves in the CMP gather do not follow a hyperbolic pattern, they do not form energy clusters in the velocity spectrum. As a result, the velocity spectrum in Figure 12d is similar to Figure 12b, with only a slight shift in the timing of the energy clusters due to the firn layer.

Figure 12e presents the velocity spectrum for the model with a sediment layer at the bottom of the subglacial lake, where the energy clusters corresponding to the primary reflections from the ice-water (R_1), water-sediment (R_2), and sediment-bedrock (R_3) interfaces are arranged from top to bottom. Following R_3, two weaker energy clusters appear, corresponding to the first-order multiples $R_2R_1R_2$ and $R_3R_1R_2$ within the water layer, with stacking velocities lower than those of the primary reflections.

3.2 Stacking

By selecting the maximum energy points of the primary reflections in each velocity spectrum, a stacking velocity model is generated for normal moveout (NMO) correction. After applying NMO, the primary reflections in the CMP gathers are flattened, while multiples retain residual moveout. Consequently, stacking the CMP gathers along the offset direction enhances the primary reflections, while the out-of-phase summation of multiples results in energy attenuation.

Figure 13a presents the stacked image of the model with absorbing boundaries. After applying NMO and stacking, the primary reflection R_1 appears as a horizontal event, indicating a flat ice-water interface. Similarly, reflection R_2 forms a horizontal event in the center of the model, suggesting a flat lake bottom. However, toward the model's edges, this event becomes inclined, indicating a gradual rise in the lake bottom near the boundaries. Below 2.5 seconds, additional reflection events emerge, stemming from the stacking of multiples $R_1R_2R_1$, which may lead to geological misinterpretations.

Similarly, Figure 13b shows the stacked section under free-surface boundary conditions. The horizontal events at 2.6s and 3.8s are first- and second-order free-surface multiples (R_1FR_1 and $R_1FR_1FR_1$) from the ice-water interface. The event at 3.3s comes from first-order interlayer multiples R_2FR_1 and R_1FR_2. Although these multiples partially reflect the characteristics of ice-water interface and lake bottom, their appearance at incorrect time depths can easily be mistaken for interfaces below the lake bottom, leading to incorrect geological interpretations. Figure 13c shows the stacked section when a firn layer is present, which closely resembling Figure 13a. This similarity arises because the energy of multiples generated at the firn-ice interface

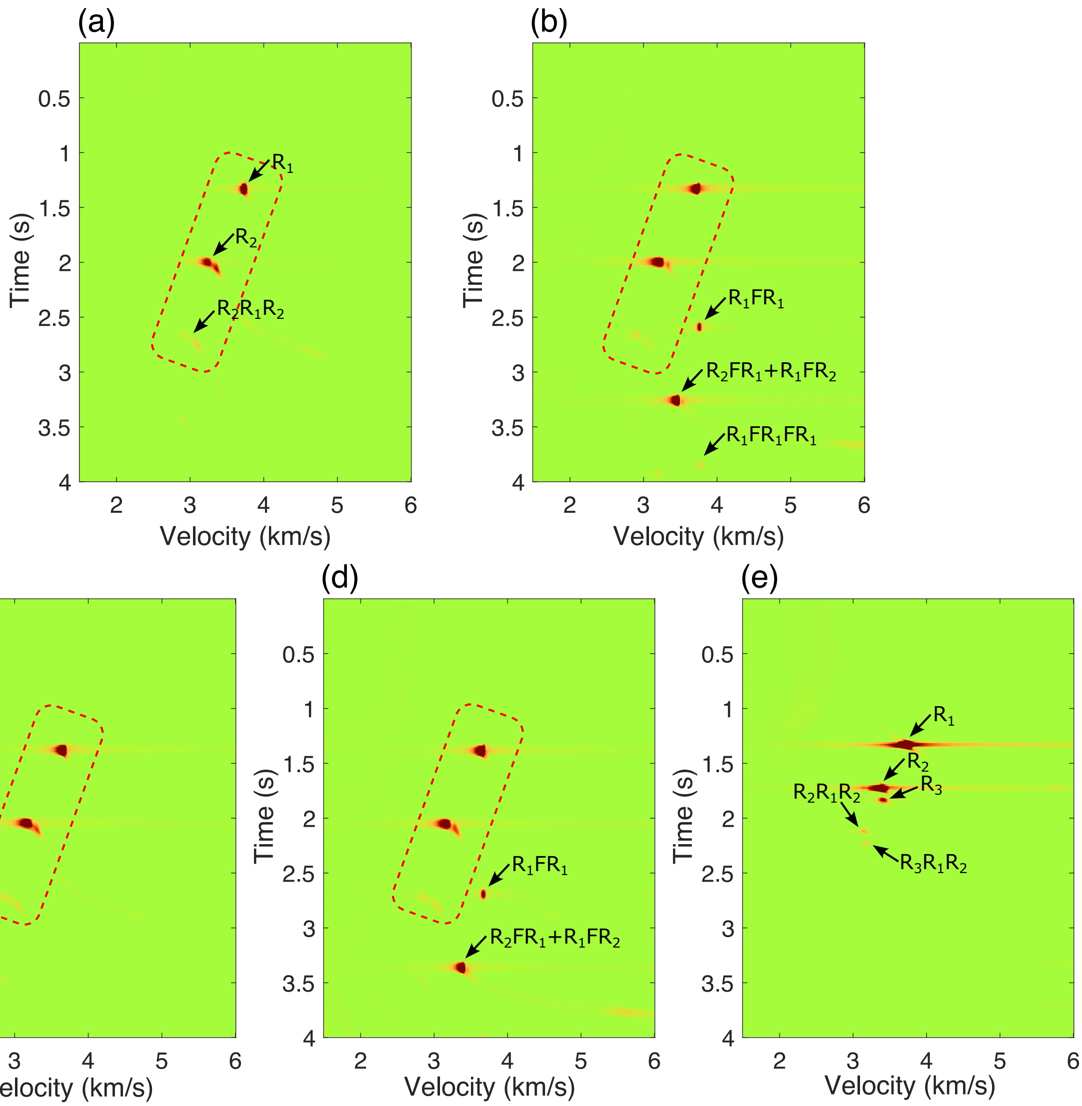

Figure 12. A velocity spectrum generated by the subglacial model, with (a) absorbing boundary, (b) free surface, (c) firn layer, (d) free surface + firn layer, and (e) sediment layer.

is weak, and out-of-phase stacking further reduces their energy, making them less visible in the stacked image. However, when both the firn layer and the free surface are present, free-surface multiples reappear more prominently.

Figure 13e presents the stacked image for the model with a sediment layer. In addition to clearly imaging the ice-water interface (R_1), water-sediment interface (R_2), and sediment-bedrock interface (R_3), the image also highlights the thinness of the sediment layer. Two horizontal seismic events between 2s and 2.5s, resembling R_2 and R_3, primarily result from the stacking of first-order interlayer multiples ($R_2R_1R_2$ and $R_3R_1R_2$), which may introduce ambiguity in geological interpretations.

https://doi.org/10.5194/egusphere-2025-646
Preprint. Discussion started: 25 March 2025
© Author(s) 2025. CC BY 4.0 License.

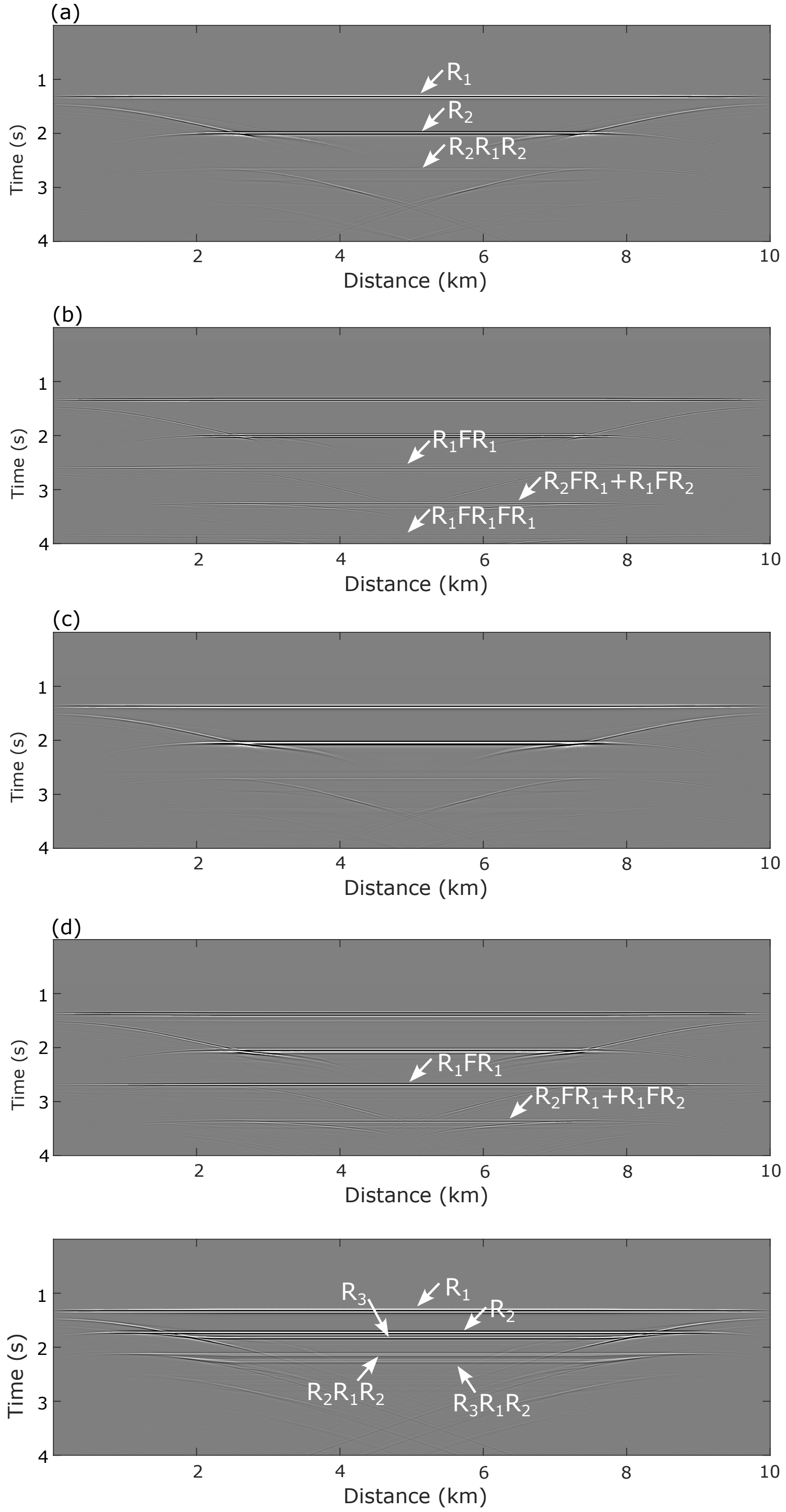

Figure 13. A stacked image of the subglacial model, with (a) absorbing boundary, (b) free surface, (c) firn layer, (d) free surface + firn layer, and (e) sediment layer.

https://doi.org/10.5194/egusphere-2025-646
Preprint. Discussion started: 25 March 2025
© Author(s) 2025. CC BY 4.0 License.

3.3 Discussion

We analyzed seismic wave propagation characteristics and data features of five subglacial models using wavefield snapshots, common shot gathers, velocity spectra, and stacked images. A key finding is the prevalent development of multiples, including free-surface and interlayer multiples within or across firn, ice, water, and sediment layers. Strong reflectors such as the free surface, ice-water, water-bedrock, and water-sediment interfaces generate high-amplitude multiples, which appear as prominent energy clusters on velocity spectra and significant events on stacked images, potentially leading to geological misinterpretations. In contrast, multiples from the firn-ice and sediment-bedrock interfaces are less pronounced due to their lower reflection coefficients.

To address these multiples, techniques such as predictive deconvolution (Sun et al., 2014) and surface-related multiple elimination (SRME) (Verschuur et al., 1992) can remove free-surface multiples from prestack gathers, while radon transform (Liu et al., 2012) can suppress interlayer multiples in angle gathers. Alternatively, multiples can be leveraged for imaging through approaches like multiple migration (Yang et al., 2015; Guo et al., 2016), full-wavefield imaging (Huang et al., 2021), or Marchenko methods (Wapenaar et al., 2014). While these techniques are well-established in the oil and gas industry, their application to subglacial environments requires further validation.

Another notable characteristic of subglacial wave propagation is the generation of guided waves when both the firn layer and the free surface are present. Although these guided waves exhibit strong energy, their weak hyperbolic features in CMP gathers result in negligible influence on the velocity spectrum and stacked images. However, as guided waves primarily propagate within the firn layer, their analysis can offer valuable insights into the detailed structure of the firn (Thiel and Ostenso, 1961).

4 Seismic acquisition system

Active-source seismic data acquisition in polar regions faces significant challenges due to harsh environmental conditions, including strong winds, extreme low temperatures, complex ice and snow cover, and limited logistical support for personnel and equipment. These factors necessitate stringent requirements for the design of seismic acquisition systems. This section presents an overview of three commonly used active-source seismic observation systems in polar regions and provides a comparative analysis of their acquisition efficiency, equipment requirements, and operational workload.

4.1 Introduction of seismic acquisition in polar area

Figure 14 depicts three types of active-source seismic acquisition systems: leap-frog Clyne et al. (2020); McMahon and Lackie (2006), snow-streamer Eisen et al. (2015), and full-coverage acquisition. Red stars indicate shot points, while blue triangles denote receiver points. The leap-frog acquisition system uses fewer receivers, resulting in shorter receiver lines. But larger offsets (source-to-receiver distances) are typically employed. In Figure 14a, the leap-frog acquisition method is illustrated: shot points are spaced at large intervals along the receiver line, starting and ending at locations distant from the line's edges. After one sequence of shots is completed, the receiver line is moved forward, and the process is repeated.

The snow-streamer acquisition system, shown in Figure 14b, typically employs longer receiver lines to achieve broader subsurface coverage. This system conducts single-sided shots, with shot points positioned at a fixed offset ahead of the receiver line. After each shot, both the shot points and receiver line advance together. A notable feature of this system is the use of gimbal-mounted geophones Van der Veen and Green (1998), which do not require ground burial. These geophones are attached to the cable and move with it, making the system well-suited for towed acquisition. In contrast, the full-coverage acquisition system, depicted in Figure 14c, involves geophones distributed across the entire survey area. Shots are fired at fixed intervals along the receiver line. This method typically requires a significantly larger number of geophones to ensure complete and uniform coverage.

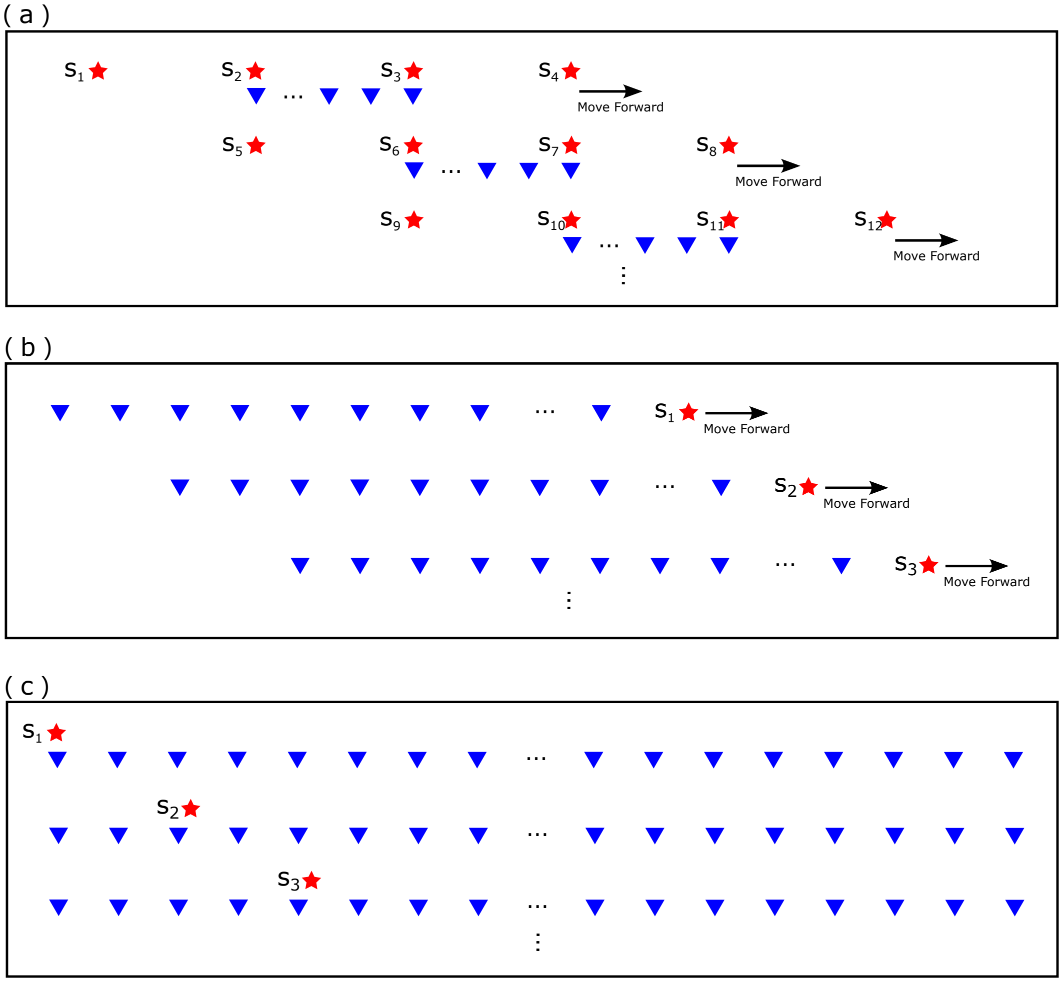

Figure 14. Comparisons of three active seismic data acquistion system, which are (a) leap-frog, (b) snow- streamer and full-coverage system.

https://doi.org/10.5194/egusphere-2025-646
Preprint. Discussion started: 25 March 2025
© Author(s) 2025. CC BY 4.0 License.

4.2 Equipment need and workload

To enable a fair comparison, all three acquisition systems are evaluated using a model with a lateral extent of 10 km and a target detection depth of 3.0 km. The geophone spacing is uniformly set to 40 meters, with coverage spanning from x = 1500 meters to x = 8500 meters. To achieve an offset-to-depth ratio of at least 1:1, the maximum offset for each system is required to exceed 2.8 km.

Table 1 summarizes the acquisition parameters for the three surveys. The leap-frog system utilizes the fewest geophones (36) but requires relocating the receiver line three times, with four shots fired per move. This results in a total workload of 160 operations, including geophone placement and shot firing. In contrast, the full-coverage acquisition system employs significantly more geophones (approximately five times that of the leap-frog system). However, as the geophones remain stationary once deployed, the workload totals 212 operations, only 32.5⊥ higher than the leap-frog system. The snow-streamer system, while requiring approximately twice the number of geophones and three times the number of shot points compared to the leap-frog system, employs towed receiver lines and gimbal-mounted geophones that do not require ground burial. Consequently, its workload is not directly comparable to the other two systems.

Table 1. Equipment need and workload of the three acquisition systems.

Acquisition type	Receiver number	Receiver starting location	Source starting location	Number of shots per move	Total shot number	Source interval per move	Line movement interval	Number of line move	minimum offset	Maximum offset
Leap frog	36	2200 m	800 m	4	16	1400 m	1400 m	3	-1400 m	2800 m
Snow streamer	69	100 m	2900 m	1	48	0	120 m	47	80 m	2800 m
Full coverage	176	1500 m	1500 m	1	36	200 m	0 m	0	0 m	7000 m

4.3 Acquisition performance

Figure 15 illustrates the coverage maps for the three acquisition systems. The leap-frog system achieves the lowest coverage due to its large shot spacing and wide line movement intervals. In comparison, the snow-streamer system, with longer receiver lines and smaller movement intervals, achieves approximately five times the coverage of the leap-frog system. As shown in Figure 15b, its coverage is evenly distributed, with linear variations at the edges and uniform coverage in the center. The full-coverage system, depicted in Figure 15c, provides the highest coverage, averaging about ten times that of the leap-frog system. This is achieved through geophones distributed across the entire survey area, resulting in a pyramid-shaped coverage map with coverage increasing linearly from the edges toward the center.

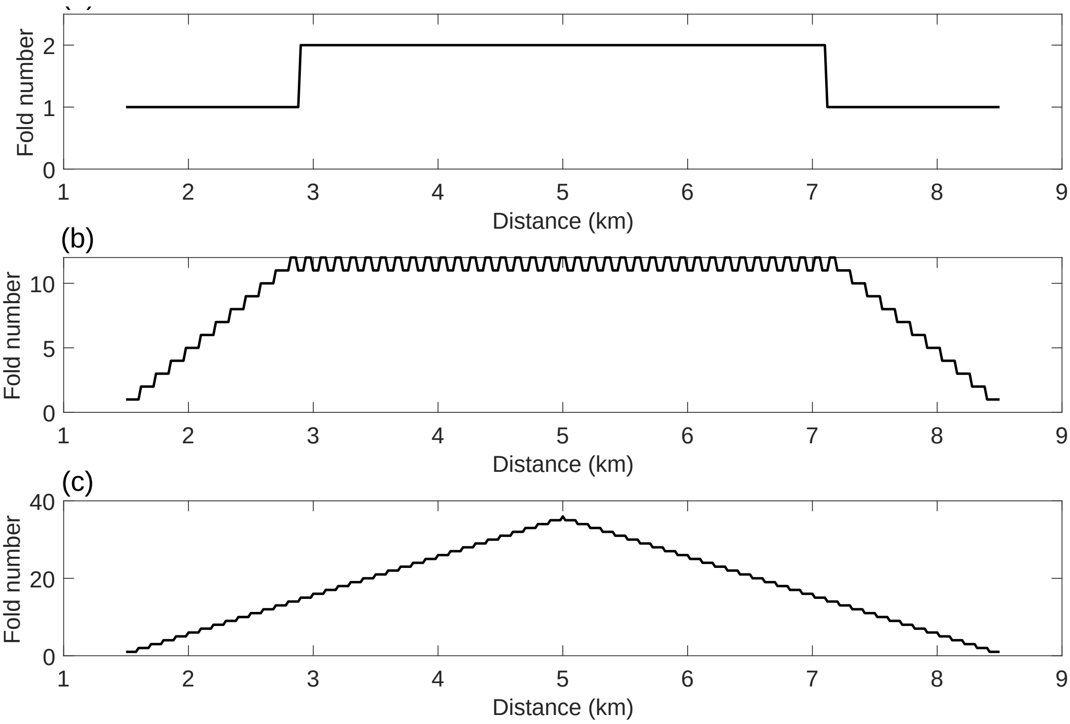

Figure 15. Fold coverage assesment of (a) leap-frog, (b) snow-streamer and (c) full-coverage acquisition system.

Beyond coverage performance, offset distribution at each CMP point is a critical factor in evaluating acquisition systems. By aggregating the offsets of all shot-receiver pairs contributing to each CMP point, the offset distribution characteristics of the three acquisition systems are analyzed, as shown in Figure 16. In each subplot, the horizontal axis represents the coverage count index, while the vertical axis denotes the offset distance.

Figure 16a illustrates that the leap-frog acquisition system not only has lower coverage counts but also exhibits significant offset variability. This uneven offset distribution poses challenges for tasks requiring detailed pre-stack seismic information, such as angle gather calculation and AVO analysis Carcione and Gei (2003), which are essential for interpreting subglacial geological structures and properties Buland and Omre (2003); Peters et al. (2008). In comparison, the snow-streamer system offers higher and more uniform offset coverage with a broader range of offsets. However, its single-sided shot configuration results in smaller offsets near x = 8020 m and larger offsets near x = 2020 m. This offset pattern may reduce vertical resolution near x = 8020 m and horizontal resolution near x = 2020 m. The full-coverage acquisition system, shown in Figure 16c, achieves excellent offset uniformity, with the offset range gradually increasing toward the center of the survey area. The maximum offset reaches 7000 m, providing extensive pre-stack variation information and enhancing resolution across the survey area.

https://doi.org/10.5194/egusphere-2025-646
Preprint. Discussion started: 25 March 2025
© Author(s) 2025. CC BY 4.0 License.

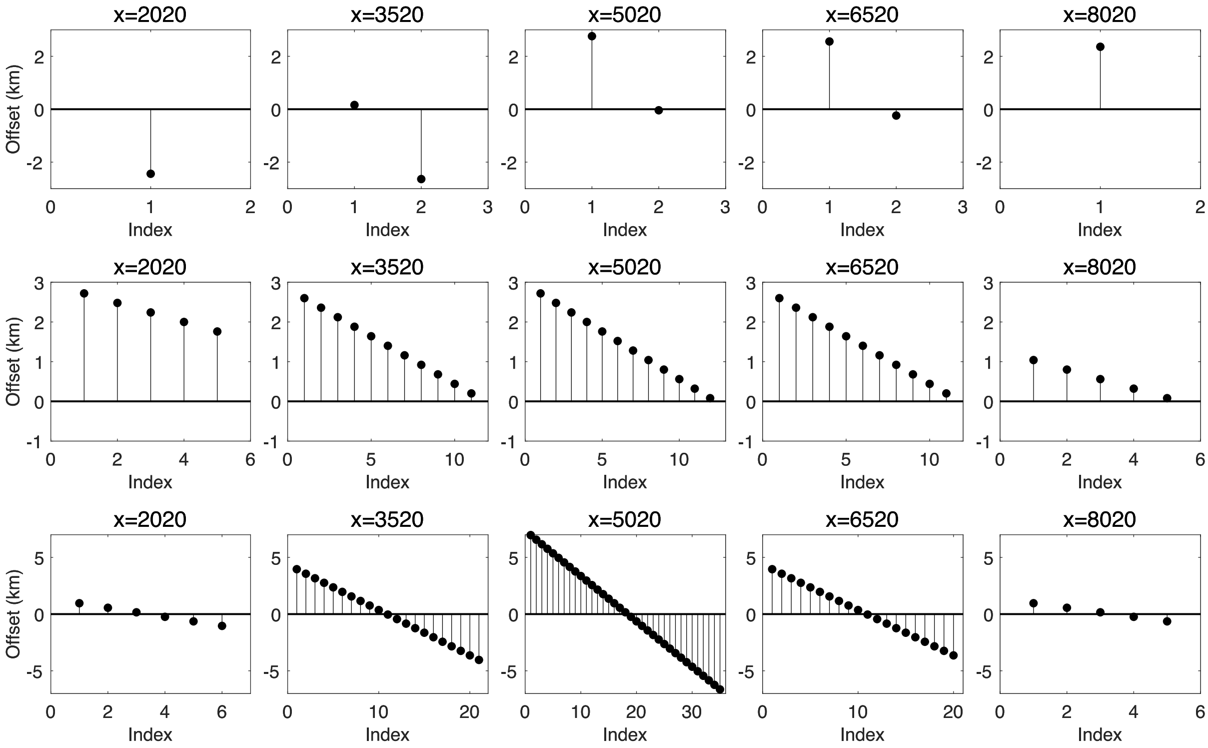

Figure 16. Assessment of the uniformity of offset distribution for (a) leap-frog, (b) snow-streamer, and (c) full-coverage acquisition systems.

4.4 Imaging quality

To assess the impact of the three acquisition systems on migration imaging, we constructed a reference reflectivity model consisting of evenly spaced diffraction points, with 200 m lateral and vertical spacing between each point. Using this reflectivity model, seismic data were generated via Born modeling, followed by reverse time migration (RTM) for imaging. Figures 17a, 17c, and 17e display the migration images corresponding to the leap-frog, snow-streamer, and full-coverage acquisition systems, respectively. The diffraction points within the water layer present the highest imaging amplitudes. This is due to the strong reflectivity of the ice-water and water-bedrock interfaces, which traps most of the seismic energy within the subglacial lake. This effect is further demonstrated through the illumination maps in Figures 17b, 17d, and 17f. Aside from concentrated energy at the shot locations, the majority of the energy is focused within the subglacial lake, providing the strongest illumination of the water layer during migration.

Figure 18 presents zoomed-in views of migration images from Figures 17a, 17c, and 17e. In the central area (blue box in Figure 18), the migrated diffraction points, or Point Spread Functions (PSFs), are consistent in shape, size, and orientation, indicating good imaging quality across all three acquisition systems. However, at the boundary (red box), the leap-frog system shows poorly focused PSFs, with noticeable tilting and stretching (white box in Figure 18a), leading to reduced horizontal resolution. The snow-streamer system improves imaging quality due to higher fold coverage and more uniform offsets, but

https://doi.org/10.5194/egusphere-2025-646
Preprint. Discussion started: 25 March 2025
© Author(s) 2025. CC BY 4.0 License.

tilting effects remain (Figure 18b). In contrast, the full-coverage system produces well-focused PSFs with minimal distortion (Figure 18c). In the deeper section (green box), the signal-to-noise ratio of the migration images improves progressively from the leap-frog to the snow-streamer system, with the full-coverage system achieving the highest quality due to increased folds and more comprehensive offset coverage.

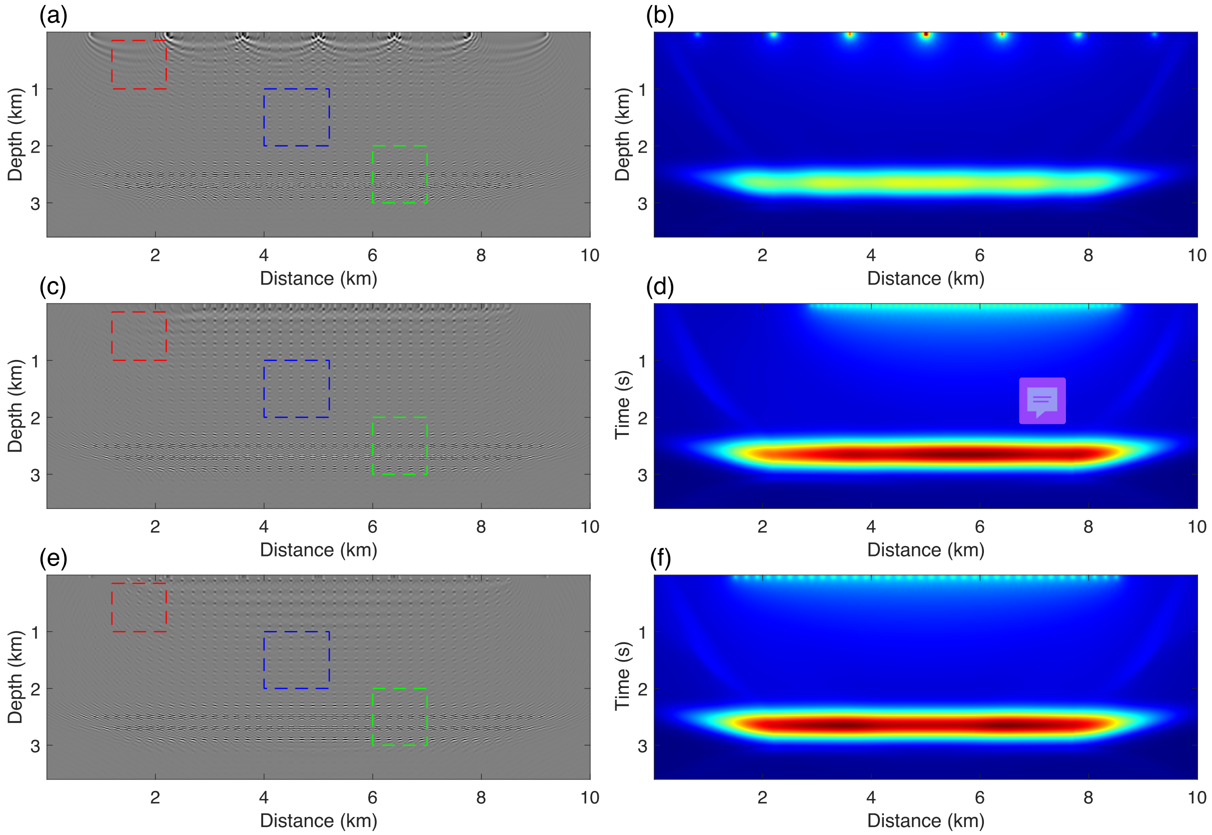

Figure 17. Evaluation of migration quality and illumination effect for (a) leap-frog, (b) snow-streamer, and (c) full-coverage acquisition systems.

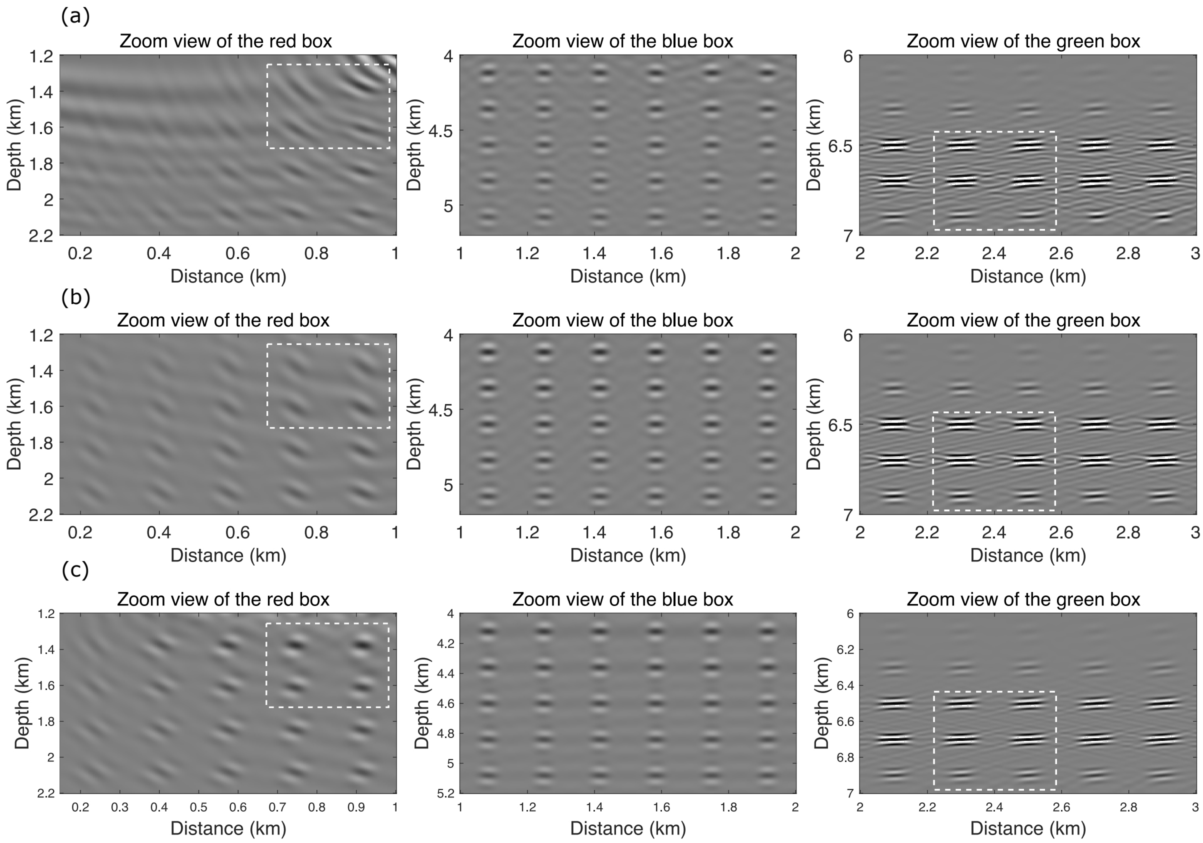

Figure 18. A zoomed-in view of the red, blue, and green boxes from (a) Figures 17a, (b) 17c, and (c) 17f, respectively.

4.5 Discussion

In summary, we introduced three common types of active seismic acquisition systems used in polar regions and compared them in terms of equipment requirements, workload, and performance. When receiver numbers are limited and the operational window is short, the leap-frog acquisition system is the fastest way to achieve full survey coverage, though it offers minimal fold numbers. These folds can be increased by reducing the line and shot intervals. The snow-streamer system, with smaller line movement intervals, demands frequent repositioning of both receiver lines and shot points, resulting in higher workloads. This system is best suited for gimbal-mounted geophones and vibroseis sources that don't require burial, reducing overall workload. However, when enough geophones are available to cover the entire survey area, the full-coverage acquisition system becomes the ideal choice for polar surveys. Its simple acquisition process, higher fold numbers, broader offset range, and more symmetrical, uniform offset coverage are advantageous for seismic migration, inversion, and prestack analyses like AVO.

In summary, this study presented and compared three common active seismic acquisition systems for polar regions, evaluating their equipment requirements, workload, and performance. The leap-frog system is suitable for achieving full survey coverage with limited receivers, but it provides the lowest fold numbers. Fold coverage can be improved by reducing line and shot intervals. When sufficient geophones are available to cover the entire survey area, the full-coverage system is the optimal choice. Its straightforward acquisition process, higher fold numbers, broader offset range, and more symmetrical and uniform offset distribution provide significant advantages for seismic migration, inversion, and prestack analyses such as AVO. The snow-streamer system is well-suited for gimbal-mounted geophones and vibroseis sources, which eliminate the need for burial and reduce operational complexity.

5 Thwaites Glacier Real Data Analysis

To validate the conclusions presented above, we analyzed and processed active-source seismic data acquired along a 9.5-km 2D seismic line on Thwaites Glacier (Muto et al., 2019; Clyne et al., 2020). These data, originally published by Clyne et al. (2020), were collected from the downstream region of Thwaites Glacier (depicted in Figure 1 of (Clyne et al., 2020)) and oriented perpendicular to the ice flow direction (referred to as the N-line).The seismic acquisition employed a leap-frog scheme, as illustrated in Figure 19, with receivers and sources alternately advancing along the seismic line. The receiver line comprised two arrays, each consisting of 48 geophones (or georods) spaced 20 meters apart and buried at a depth of 20 cm. Source points were distributed along the line and activated at non-uniform intervals. After each round of source activations, the receiver line was advanced 940 meters, followed by the next round of shots. Explosive sources, ranging in charge size from 175 to 400 grams, were detonated in boreholes at depths between 96 meters and near the surface.

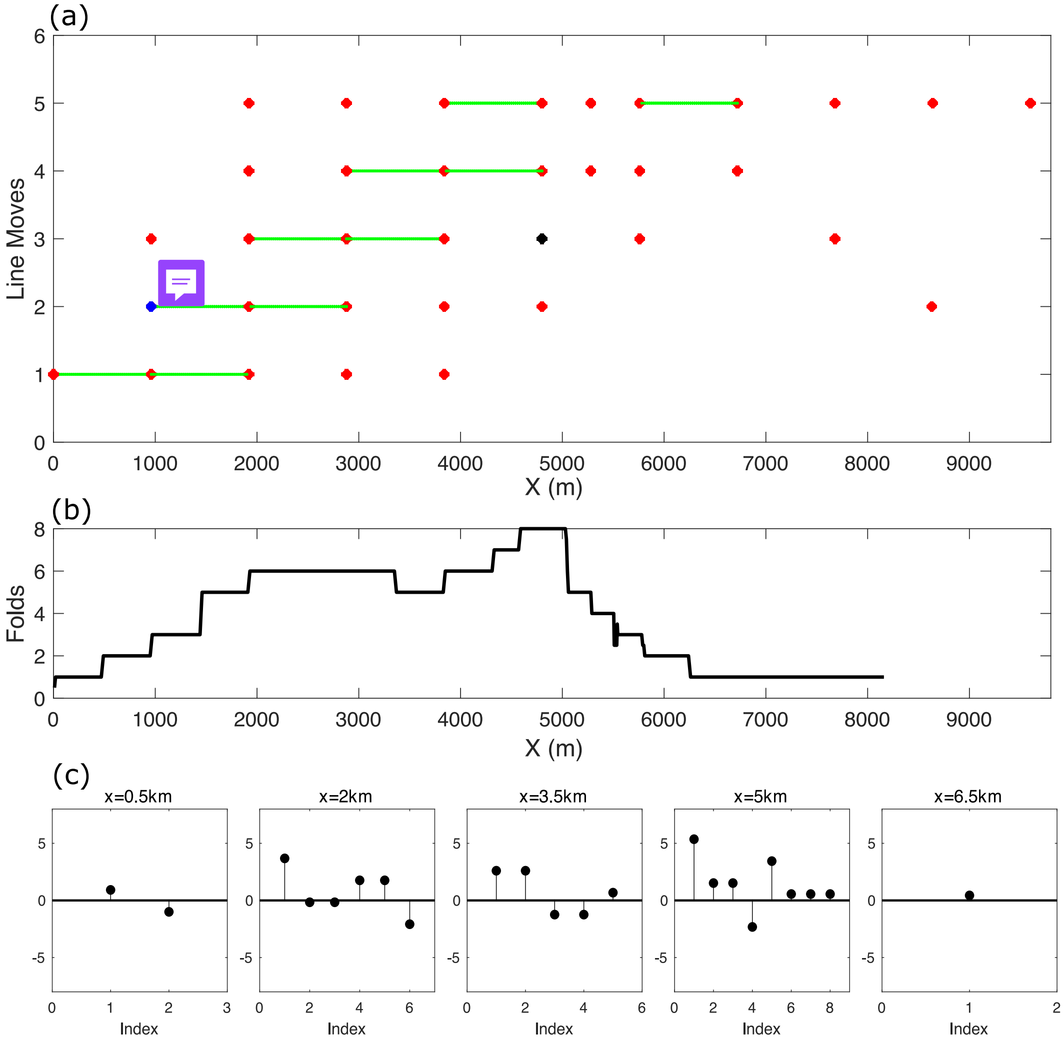

Figure 19. Acquisition geometry of the N-line data, where sources move along the line in a leap frogging manner. Colored stars represent the source positions, while green dots indicate the receiver positions.

The seismic data were recorded for 4 seconds with a sampling interval of 0.25 milliseconds. Figure 20 shows two common shot gathers (CSGs), with source locations marked by blue and black stars in Figure 19. Strong guided waves are evident in the shallow time region, consistent with the simulations in Section 2.4, resulting from multiple total reflections within the firn layer caused by the free surface and the firn-ice interface. A clear primary reflection from the ice-bedrock interface is observed between 1 and 1.5 seconds, aligning with the results in Section 2.1. First-order free-surface multiples from the ice-bedrock interface are visible around 2.5 seconds, with travel times approximately double those of the primary reflections, consistent with Section 2.2. As this seismic line does not intersect subglacial lakes or sedimentary layers, no multiples associated with these features are observed in the seismic records in Figure 20.

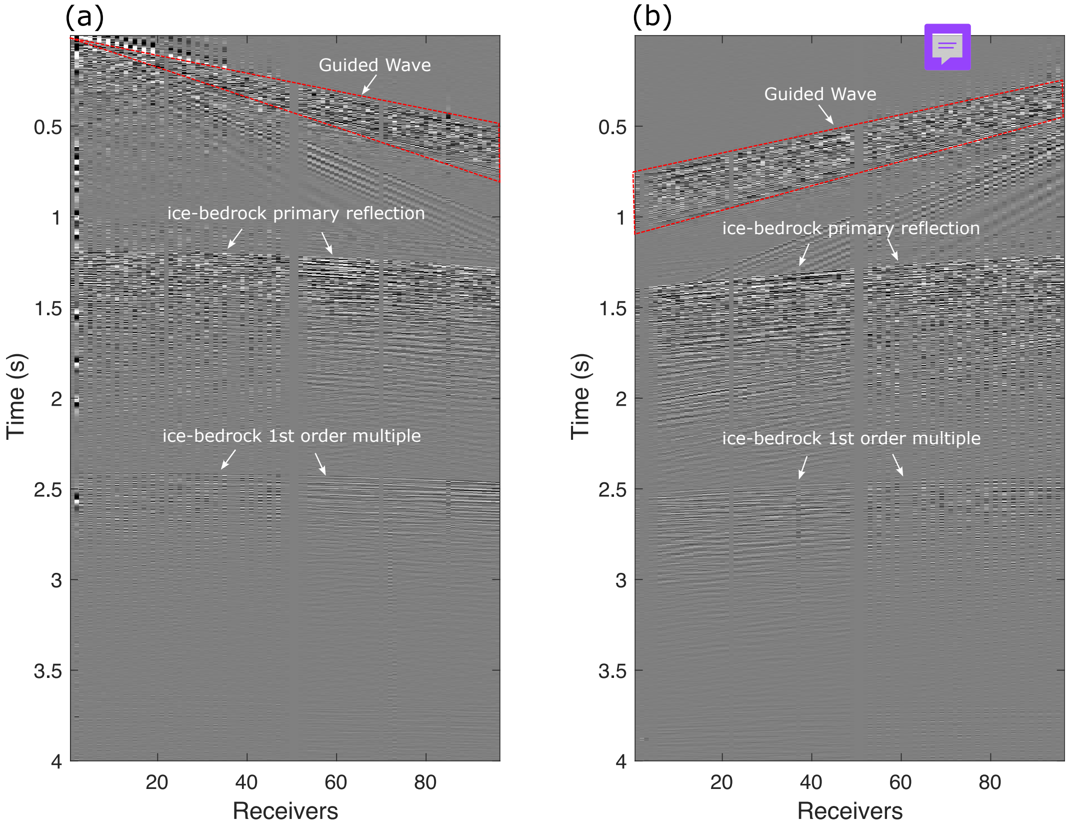

Figure 20. Acquisition geometry of the N-line data, where sources move along the line in a leap frogging manner. Colored stars represent the source positions, while green dots indicate the receiver positions.

The seismic data were processed using a constant velocity of 3850 m/s for NMO correction and stacking, with the results shown in Figure 21a. A continuous reflection event corresponding to the primary reflection from the ice-bedrock interface is observed at approximately $t = 1.2$ s. Around $t = 2.4$ s, a second event caused by first-order free-surface multiples from the ice-bedrock interface is identified, consistent with the simulation results in Figure 13a. Although this event has low amplitude, it may introduce artifacts into seismic interpretation.

Figure 21b provides a zoomed-in view of the red-boxed area in Figure 21a. Approximately 0.05 s below the primary reflection, a similar event with inverted polarity is observed (red dashed line). This phenomenon is often attributed to velocity anomalies beneath the ice-bedrock interface that reverse the reflection coefficients at their boundaries. However, no interlayer multiples associated with velocity anomalies were detected in the prestack or stacked data, invalidating this hypothesis. Further analysis identifies this event as a source-side ghost multiple Kiraz et al. (2024). The upper-right inset of Figure 21b illustrates the difference in wave paths between the source-side ghost multiple (red solid line) and the primary reflection (green solid line). The ghost multiple is caused by deep source depths (up to 96 m), where the wave reflects upward at the free surface

© Author(s) 2025. CC BY 4.0 License.

before propagating downward, resulting in a phase reversal. This mechanism is analogous to source-side ghost generation in marine streamer acquisition.

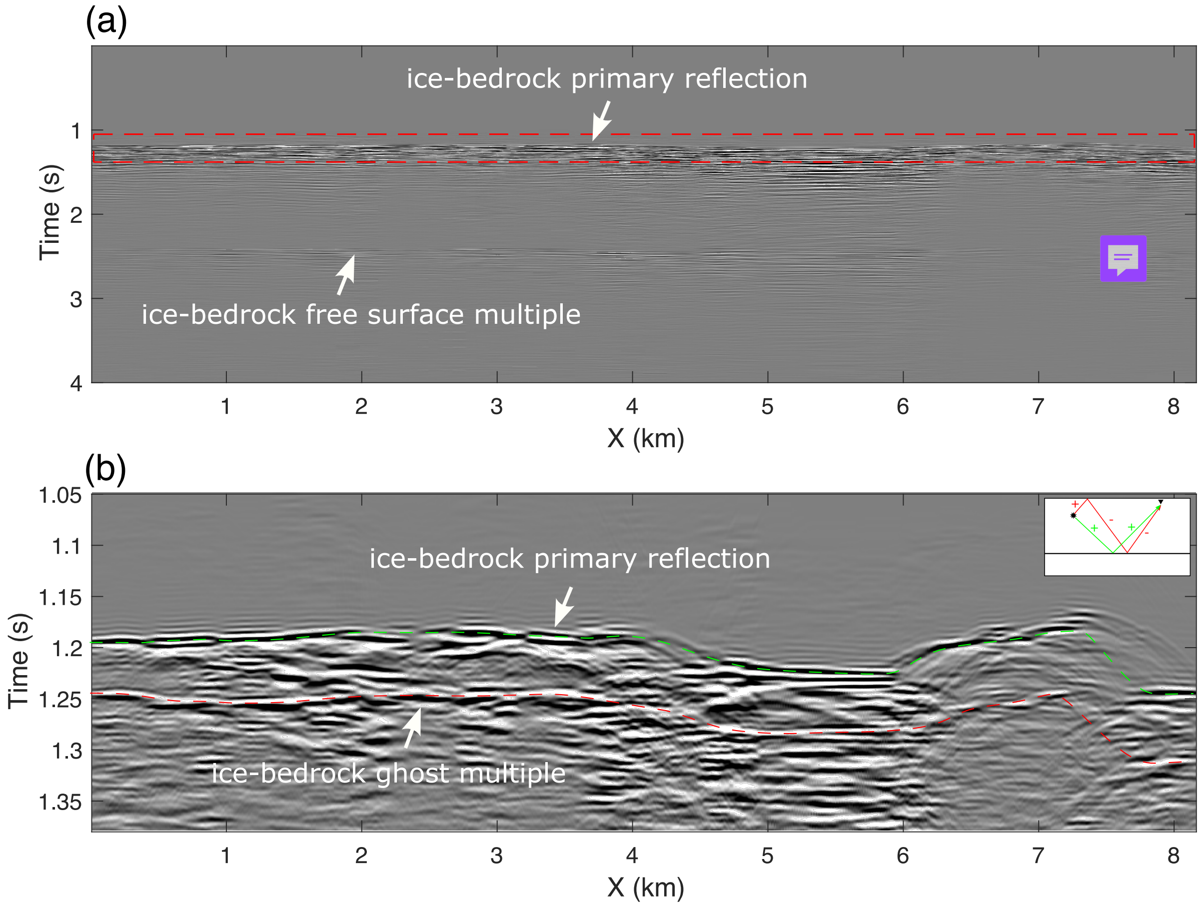

Figure 21. Acquisition geometry of the N-line data, where sources move along the line in a leap frogging manner. Colored stars represent the source positions, while green dots indicate the receiver positions.

To obtain the true spatial distribution of subsurface interfaces, we applied reverse time migration (RTM) to the prestack seismic data, resulting in the migrated image shown in Figure 22a. The ice-bedrock interface appears at approximately $z = 2.4$ km, while the interface at $z = 4.8$ km corresponds to the imaging of first-order free-surface multiples. Figure 22b shows a zoomed-in view of the red-boxed area in Figure 22a, where the seismic layers marked by the green and red dashed lines indicate the imaging results of the ice-bedrock primary reflection and the source-side ghost multiple, respectively. Similar to the stacked image, the two interfaces exhibit similar amplitudes but opposite phases. Although the migration image offers higher resolution compared to the stacked image, significant migration artifacts are observed, which due to the limited fold coverage of the acquisition system (Figure 19b). This issue is particularly severe in the region between $x = 6$ km and $x = 8$ km, where the coverage is as low as 1. Additionally, the ice-bedrock layer are absent in the ranges of $x = 4.4 \sim 4.6$ km and

https://doi.org/10.5194/egusphere-2025-646
Preprint. Discussion started: 25 March 2025
© Author(s) 2025. CC BY 4.0 License.

$x = 6 \sim 6.5$ km, potentially corresponding to steeply dipping interfaces. This phenomenon is caused by the uneven distribution 380 of offsets in the acquisition system (Figure 19c), particularly the lack of far-offset data, which significantly affects the imaging of steeply dipping structures. These observations are consistent with the simulation results shown in Figures 17a and 18a.

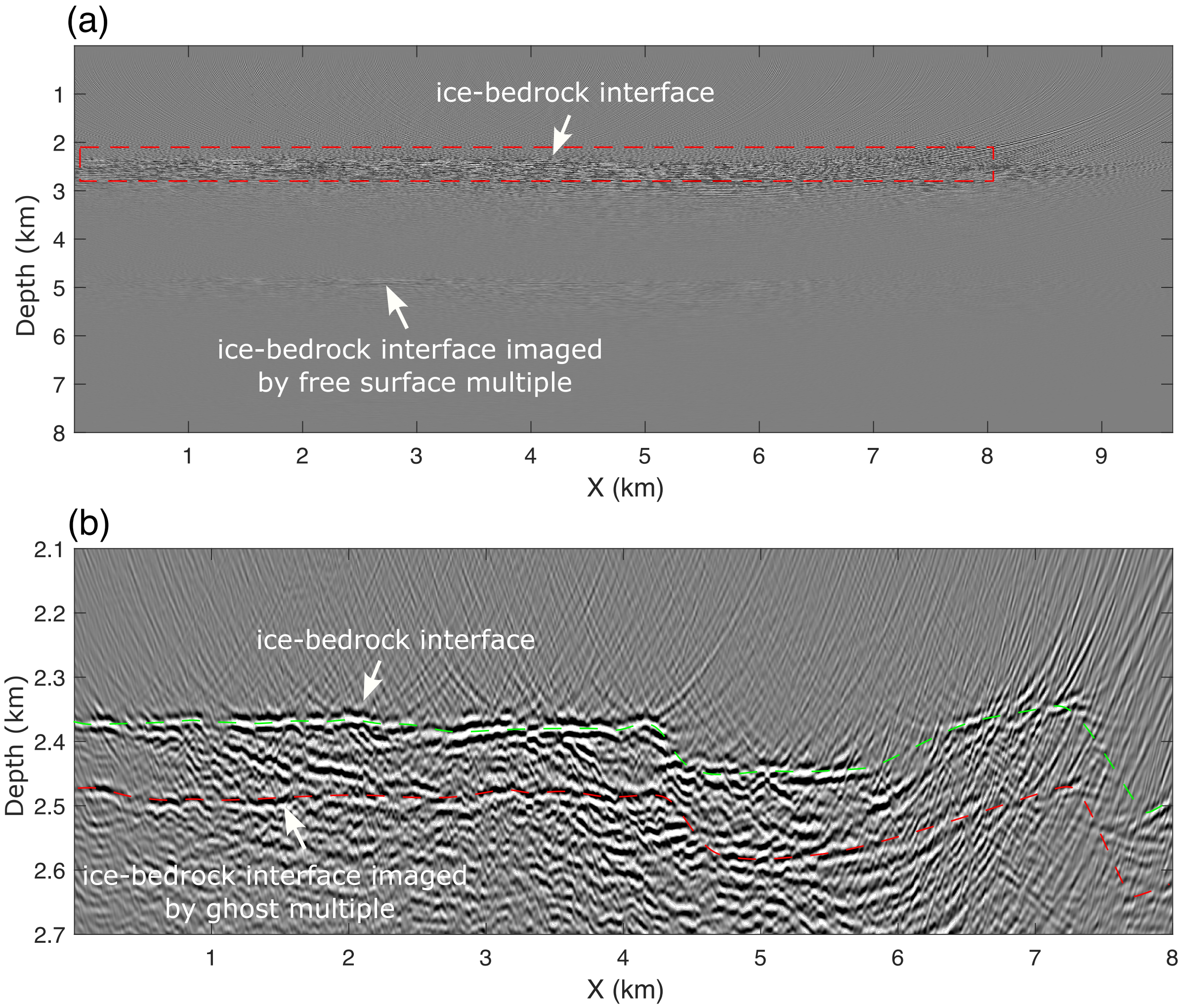

Figure 22. Acquisition geometry of the N-line data, where sources move along the line in a leap frogging manner. Colored stars represent the source positions, while green dots indicate the receiver positions.

6 Conclusions

Active-source seismic exploration of subglacial lakes has a long history, but its application remains limited due to Antarctica's extreme environment, and studies on the seismic wavefield characteristics of these structures are even rarer. This study 385 established a representative subglacial lake model and systematically analyzed the wavefield characteristics, data processing

© Author(s) 2025. CC BY 4.0 License.

challenges, and optimal acquisition system design. Beyond supporting seismic exploration of Lake Qilin, the findings also provide theoretical guidance for broader subglacial lake investigations. The wavefield simulation results reveal two key features: (1) the prevalence of multiple reflections, including those within the water and sediment layers, snow-ice interface multiples, free-surface multiples, and mixed multiples across various interfaces; and (2) the significant presence of guided waves in the shallow firn layer.

Conventional seismic data processing workflows, including velocity analysis, dynamic correction, and stacking, were applied to the simulated data. The velocity spectrum reveals the following: (1) the presence of multiples significantly increases spectral complexity, posing challenges for accurate velocity estimation; (2) the stacking velocity of the primary reflection from the water-bedrock interface (v_1) is notably lower than that of the ice-water interface (v_2), reflecting the slower velocity of the water layer; and (3) free-surface multiples exhibit stacking velocities between v_1 and v_2, while interlayer multiples within the water and sediment layers typically have stacking velocities below v_1; (4) although guided waves exhibit strong energy, they fail to align coherently after dynamic correction and cannot be effectively stacked, rendering their contribution negligible in the velocity spectrum. In stacked images, the amplitudes of coherent events from multiples are weaker than those of primary reflections. However, these multiple-related events may introduce geological artifacts, potentially leading to misinterpretations.

The handling of multiples represents a key challenge in the seismic processing of subglacial lake data, encompassing two critical aspects: (1) Separation of multiples from primary reflections: Effective separation enables the application of conventional seismic processing techniques to datasets containing only primary reflections; and (2) Direct imaging of multiples: Traditionally considered noise, multiples hold significant potential for super-resolution imaging. While the resolution limit for primary reflections is $\lambda/4$, multiples can achieve resolutions of $\lambda/8$ or higher due to their sensitivity to small-scale subsurface anomalies. In addition to multiples, the processing of guided waves presents another challenge. Although guided waves cannot directly image subglacial lakes or deeper structures, they carry critical velocity information from the firn layer, which is essential for accurate deep imaging. The travel time and dispersion characteristics of guided waves provide valuable constraints for inverting the firn layer velocity model. Furthermore, complementary datasets, including radar observations and ice core analyses from drilling, can provide critical constraints to improve the accuracy and reliability of seismic processing.

Considering the harsh environment and the limited active-source data acquisition window in antartica, a key challenge in seismic acquisition is designing an observation system that can achieve the maximum number of coverage in the shortest time. This paper evaluates three observation systems, leap-frog, snow-streamer, and full-coverage, across five factors: equipment quantity, workload, fold coverage, offset distribution, and imaging quality. The analysis shows that the leap-frog system requires the fewest geophones and minimal workload but offers the lowest fold coverage, the least uniform offset distribution, and the poorest imaging results. In contrast, the full-coverage system requires approximately five times as many geophones as the leap-frog system, but only results in a 30 ⊥ increase in workload and achieves approximately ten times the fold coverage. Additionally, it provides the most uniform offset distribution and the best imaging quality. The snow-streamer system falls between the leap-frog and full-coverage systems in performance. However, its common use of gimbal-mounted geophones, which only record vertical ground motion, limits its effectiveness in shear-wave detection. Three-component nodal geophones are expected to remain the preferred equipment for active-source seismic surveys in antartica for the foreseeable future.

© Author(s) 2025. CC BY 4.0 License.

Finally, we analyzed and processed the 2D active-source seismic data collected from Thwaites Glacier. Although there is no subglacial lake beneath the survey line, which prevents full verification of the alignment between the data features and the simulation results, several observations can still be made. First, the data clearly exhibits free-surface multiples and guided waves, which are consistent with the conclusions in Sections 2.2 and 2.4. Second, after stacking the multiples, their energy remains in the stacked image. Their shape is similar to that of primary reflections, but they appear at greater depths, which aligns with the conclusions in Section 3.2. Finally, due to the use of the leap-frog observation system, the maximum coverage is only 8 times, and in the 6-8 km range, the fold number is just one. This low coverage leads to noticeable migration artifacts in the migration image, which is consistent with the analysis in Section 4.3.

To streamline the analysis, this study uses the acoustic wave equation. However, to capture a more comprehensive wavefield, additional physical parameters could be considered in the subglacial lake model. For example, the porosity of the firn layer and the meltwater within it may cause seismic wave attenuation, which could be addressed by using a viscous wave equation Hao and Greenhalgh (2019); Agnew et al. (2023); Picotti et al. (2024). Additionally, shear waves are likely to propagate through the ice sheet and bedrock, suggesting the potential use of an elastic wave equation Virieux (1986). The anisotropic nature of the ice sheet, due to its layering, could also be an important factorAlkhalifah (2000); Llorens et al. (2020). These considerations will be explored in future work, where the simulation results will be further validated using active-source seismic data from Lake Qilin.

Author contributions. Kai Lu conceived the study, designed the experiment, and drafted the manuscript. Yuqing Chen conducted the simulations and revised the manuscript.

Competing interests. The authors declare that they have no competing interests.

Acknowledgements. This work was supported by the National Key Research and Development Program of China (2023YFC2812601). The authors gratefully acknowledge the computational resources provided by the High-performance Computing Platform at China University of Geosciences, Beijing.

References

Firn on ice sheets, Nature Reviews Earth & Environment, 5, 79–99, 2024.

Agnew, R. S., Clark, R. A., Booth, A. D., Brisbourne, A. M., and Smith, A. M.: Measuring seismic attenuation in polar firn: method and application to Korff Ice Rise, West Antarctica, Journal of Glaciology, pp. 1–12, 2023.

Alkhalifah, T.: An acoustic wave equation for anisotropic media, Geophysics, 65, 1239–1250, 2000.

Anandakrishnan, S. and Winberry, J.: Antarctic subglacial sedimentary layer thickness from receiver function analysis, Global and Planetary Change, 42, 167–176, 2004.

Bentley, M., Christoffersen, P., Hodgson, D., Smith, A., Tulaczyk, S., and Le Brocq, A.: Subglacial lake sediments and sedimentary processes: potential archives of ice sheet evolution, past environmental change, and the presence of life, Antarctic subglacial aquatic environments, 192, 83–110, 2011.

Boiero, D., Wiarda, E., and Vermeer, P.: Surface-and guided-wave inversion for near-surface modeling in land and shallow marine seismic data, The Leading Edge, 32, 638–646, 2013.

Buland, A. and Omre, H.: Bayesian linearized AVO inversion, Geophysics, 68, 185–198, 2003.

Carcione, J. M. and Gei, D.: Seismic modelling study of a subglacial lake, Geophysical prospecting, 51, 501–515, 2003.

Chaput, J., Aster, R., Karplus, M., and Nakata, N.: Ambient high-frequency seismic surface waves in the firn column of central west Antarctica, Journal of Glaciology, 68, 785–798, 2022.

Chen, Y., Feng, Z., Fu, L., AlTheyab, A., Feng, S., and Schuster, G.: Multiscale reflection phase inversion with migration deconvolution, Geophysics, 85, R55–R73, 2020.

Christner, B. C., Priscu, J. C., Achberger, A. M., Barbante, C., Carter, S. P., Christianson, K., Michaud, A. B., Mikucki, J. A., Mitchell, A. C., Skidmore, M. L., et al.: A microbial ecosystem beneath the West Antarctic ice sheet, Nature, 512, 310–313, 2014.

Clyne, E. R., Anandakrishnan, S., Muto, A., Alley, R. B., and Voigt, D. E.: Interpretation of topography and bed properties beneath Thwaites Glacier, West Antarctica using seismic reflection methods, Earth and Planetary Science Letters, 550, 116 543, 2020.

Contributors, W.: East Antarctic Ice Sheet, https://en.wikipedia.org/wiki/East_Antarctic_Ice_Sheet?utm_source=chatgpt.com, accessed: 2024-01-24, 2024.

Cui, X., Greenbaum, J. S., Beem, L. H., Guo, J., Ng, G., Li, L., Blankenship, D., and Sun, B.: The first fixed-wing aircraft for Chinese Antarctic expeditions: Airframe, modifications, scientific instrumentation and applications, Journal of Environmental and Engineering Geophysics, 23, 1–13, 2018.

Cui, X., Greenbaum, J. S., Lang, S., Zhao, X., Li, L., Guo, J., and Sun, B.: The scientific operations of Snow Eagle 601 in Antarctica in the past five austral seasons, Remote Sensing, 12, 2994, 2020a.

Cui, X., Jeofry, H., Greenbaum, J. S., Guo, J., Li, L., Lindzey, L. E., Habbal, F. A., Wei, W., Young, D. A., Ross, N., et al.: Bed topography of princess Elizabeth land in east Antarctica, Earth System Science Data, 12, 2765–2774, 2020b.

Diez, A., Eisen, O., Hofstede, C., Bohleber, P., and Polom, U.: Joint interpretation of explosive and vibroseismic surveys on cold firn for the investigation of ice properties, Annals of Glaciology, 54, 201–210, 2013.

Eisen, O., Hofstede, C., Diez, A., Kristoffersen, Y., Lambrecht, A., Mayer, C., Blenkner, R., and Hilmarsson, S.: On-ice vibroseis and snowstreamer systems for geoscientific research, Polar Science, 9, 51–65, 2015.

Filina, I., Lukin, V., Masolov, V., and Blankenship, D.: Unconsolidated sediments at the bottom of Lake Vostok from seismic data, US Geological Survey and The National Academies Short Research Paper, 31, 2007.

© Author(s) 2025. CC BY 4.0 License.

Garcia-Lopez, E. and Cid, C.: Glaciers and ice sheets as analog environments of potentially habitable icy worlds, Frontiers in microbiology, 8, 1407, 2017.

Glaciers, A.: East Antarctic Ice Sheet, https://www.antarcticglaciers.org/antarctica-2/east-antarctic-ice-sheet/, accessed: 2024-01-24, 2024.

Guo, B., Huang, Y., Røstad, A., and Schuster, G.: Far-field super-resolution imaging of resonant multiples, Science advances, 2, e1501 439, 2016.

Hao, Q. and Greenhalgh, S.: The generalized standard-linear-solid model and the corresponding viscoacoustic wave equations revisited, Geophysical Journal International, 219, 1939–1947, 2019.

Hollmann, H., Treverrow, A., Peters, L. E., Reading, A. M., and Kulessa, B.: Seismic observations of a complex firn structure across the Amery Ice Shelf, East Antarctica, Journal of Glaciology, 67, 777–787, 2021.

Horgan, H. J., Anandakrishnan, S., Jacobel, R. W., Christianson, K., Alley, R. B., Heeszel, D. S., Picotti, S., and Walter, J. I.: Subglacial Lake Whillans—Seismic observations of a shallow active reservoir beneath a West Antarctic ice stream, Earth and Planetary Science Letters, 331, 201–209, 2012.

Huang, R., Zhang, Z., Wu, Z., Wei, Z., Mei, J., and Wang, P.: Full-waveform inversion for full-wavefield imaging: Decades in the making, The Leading Edge, 40, 324–334, 2021.

Jamieson, S. S., Ross, N., Paxman, G. J., Clubb, F. J., Young, D. A., Yan, S., Greenbaum, J., Blankenship, D. D., and Siegert, M. J.: An ancient river landscape preserved beneath the East Antarctic Ice Sheet, Nature Communications, 14, 6507, 2023.

Joughin, I. and Alley, R. B.: Stability of the West Antarctic ice sheet in a warming world, Nature Geoscience, 4, 506–513, 2011.

Kiraz, M. S., Snieder, R., and Sheiman, J.: Attenuating free-surface multiples and ghost reflection from seismic data using a trace-by-trace convolutional neural network approach, Geophysical Prospecting, 72, 908–937, 2024.

Lan, H. and Zhang, Z.: Comparative study of the free-surface boundary condition in two-dimensional finite-difference elastic wave field simulation, Journal of Geophysics and Engineering, 8, 275, 2011.

Li, J., Hanafy, S., and Schuster, G.: Wave-equation dispersion inversion of guided P waves in a waveguide of arbitrary geometry, Journal of Geophysical Research: Solid Earth, 123, 7760–7774, 2018.

Li, Y., Shi, H., Lu, Y., Zhang, Z., and Xi, H.: Subglacial discharge weakens the stability of the Ross Ice Shelf around the grounding line, Polar Research, 40, 2021.

Liu, Z., Zhao, W., and Zhu, Z.: Multiple attenuation using multichannel predictive deconvolution in radial domain, in: SEG International Exposition and Annual Meeting, pp. SEG–2012, SEG, 2012.

Livingstone, S., Clark, C., Woodward, J., and Kingslake, J.: Potential subglacial lakes and meltwater drainage pathways beneath the Antarctic and Greenland ice sheets, The Cryosphere, 7, 1721–1740, 2013.

Livingstone, S. J., Li, Y., Rutishauser, A., Sanderson, R. J., Winter, K., Mikucki, J. A., Björnsson, H., Bowling, J. S., Chu, W., Dow, C. F., et al.: Subglacial lakes and their changing role in a warming climate, Nature Reviews Earth & Environment, 3, 106–124, 2022.

Llorens, M.-G., Griera, A., Bons, P. D., Gomez-Rivas, E., Weikusat, I., Prior, D. J., Kerch, J., and Lebensohn, R. A.: Seismic anisotropy of temperate ice in polar ice sheets, Journal of Geophysical Research: Earth Surface, 125, e2020JF005 714, 2020.

Luo, S. and Hale, D.: Velocity analysis using weighted semblance, Geophysics, 77, U15–U22, 2012.

Maguire, R., Schmerr, N., Pettit, E., Riverman, K., Gardner, C., DellaGiustina, D. N., Avenson, B., Wagner, N., Marusiak, A. G., Habib, N., et al.: Geophysical constraints on the properties of a subglacial lake in northwest Greenland, The Cryosphere, 15, 3279–3291, 2021.

McMahon, K. L. and Lackie, M. A.: Seismic reflection studies of the Amery Ice Shelf, East Antarctica: delineating meteoric and marine ice, Geophysical Journal International, 166, 757–766, 2006.

Mikucki, J. A., Lee, P., Ghosh, D., Purcell, A., Mitchell, A. C., Mankoff, K., Fisher, A., Tulaczyk, S., Carter, S., Siegfried, M. R., et al.: Subglacial Lake Whillans microbial biogeochemistry: a synthesis of current knowledge, Philosophical Transactions of the Royal Society A: Mathematical, Physical and Engineering Sciences, 374, 20140 290, 2016.

Muto, A., Anandakrishnan, S., Alley, R. B., Horgan, H. J., Parizek, B. R., Koellner, S., Christianson, K., and Holschuh, N.: Relating bed character and subglacial morphology using seismic data from Thwaites Glacier, West Antarctica, Earth and Planetary Science Letters, 507, 199–206, 2019.

Napoleoni, F., Jamieson, S. S., Ross, N., Bentley, M. J., Rivera, A., Smith, A. M., Siegert, M. J., Paxman, G. J., Gacitúa, G., Uribe, J. A., et al.: Subglacial lakes and hydrology across the Ellsworth subglacial highlands, West Antarctica, The Cryosphere, 14, 4507–4524, 2020.

Pattyn, F., Carter, S. P., and Thoma, M.: Advances in modelling subglacial lakes and their interaction with the Antarctic ice sheet, Philosophical Transactions of the Royal Society A: Mathematical, Physical and Engineering Sciences, 374, 20140 296, 2016.

Pearce, E., Booth, A. D., Rost, S., Sava, P., Konuk, T., Brisbourne, A., Hubbard, B., and Jones, I.: A synthetic study of acoustic full waveform inversion to improve seismic modelling of firn, Annals of Glaciology, 63, 44–48, 2022.

Peters, L., Anandakrishnan, S., Holland, C., Horgan, H., Blankenship, D., and Voigt, D.: Seismic detection of a subglacial lake near the South Pole, Antarctica, Geophysical Research Letters, 35, 2008.

Picotti, S., Carcione, J. M., and Pavan, M.: Seismic attenuation in Antarctic firn, The Cryosphere, 18, 169–186, 2024.

Schlegel, R., Diez, A., Löwe, H., Mayer, C., Lambrecht, A., Freitag, J., Miller, H., Hofstede, C., and Eisen, O.: Comparison of elastic moduli from seismic diving-wave and ice-core microstructure analysis in Antarctic polar firn, Annals of Glaciology, 60, 220–230, 2019.

Siegert, M. J.: A 60-year international history of Antarctic subglacial lake exploration, 2018.

Siegert, M. J., Ross, N., and Le Brocq, A. M.: Recent advances in understanding Antarctic subglacial lakes and hydrology, Philosophical Transactions of the Royal Society A: Mathematical, Physical and Engineering Sciences, 374, 20140 306, 2016.

Siegfried, M., Venturelli, R., Patterson, M., Arnuk, W., Campbell, T., Gustafson, C., Michaud, A., Galton-Fenzi, B., Hausner, M., Holzschuh, S., et al.: The life and death of a subglacial lake in West Antarctica, Geology, 51, 434–438, 2023.

Siegfried, M. R. and Fricker, H. A.: Thirteen years of subglacial lake activity in Antarctica from multi-mission satellite altimetry, Annals of Glaciology, 59, 42–55, 2018.

Smith, A. M., Woodward, J., Ross, N., Bentley, M. J., Hodgson, D. A., Siegert, M. J., and King, E. C.: Evidence for the long-term sedimentary environment in an Antarctic subglacial lake, Earth and Planetary Science Letters, 504, 139–151, 2018.

Stearns, L. A., Smith, B. E., and Hamilton, G. S.: Increased flow speed on a large East Antarctic outlet glacier caused by subglacial floods, Nature Geoscience, 1, 827–831, 2008.

Sun, W., Hu, J., Wang, H., and Liu, S.: Separate Multiple and Primary with Sparse Constraints in Local Tau-p domain, in: Beijing 2014 International Geophysical Conference & Exposition, Beijing, China, 21-24 April 2014, pp. 352–354, Society of Exploration Geophysicists and Chinese Petroleum Society, 2014.

Thiel, E. and Ostenso, N. A.: Seismic studies on Antarctic ice shelves, Geophysics, 26, 706–715, 1961.

Van der Veen, M. and Green, A. G.: Land streamer for shallow seismic data acquisition: Evaluation of gimbal-mounted geophones, Geophysics, 63, 1408–1413, 1998.

Verschuur, D. J., Berkhout, A., and Wapenaar, C.: Adaptive surface-related multiple elimination, Geophysics, 57, 1166–1177, 1992.

Vick-Majors, T. J., Michaud, A. B., Skidmore, M. L., Turetta, C., Barbante, C., Christner, B. C., Dore, J. E., Christianson, K., Mitchell, A. C., Achberger, A. M., et al.: Biogeochemical connectivity between freshwater ecosystems beneath the West Antarctic Ice Sheet and the sub-ice marine environment, Global Biogeochemical Cycles, 34, no–no, 2020.

Virieux, J.: P-SV wave propagation in heterogeneous media: Velocity-stress finite-difference method, Geophysics, 51, 889–901, 1986.

Wapenaar, K., Thorbecke, J., Van Der Neut, J., Broggini, F., Slob, E., and Snieder, R.: Marchenko imaging, Geophysics, 79, WA39–WA57, 2014.

Winberry, J. P., Anandakrishnan, S., and Alley, R. B.: Seismic observations of transient subglacial water-flow beneath MacAyeal Ice Stream, West Antarctica, Geophysical Research Letters, 36, 2009.

Wingham, D. J., Siegert, M. J., Shepherd, A., and Muir, A. S.: Rapid discharge connects Antarctic subglacial lakes, Nature, 440, 1033–1036, 2006.

Yan, P., Li, Z., Li, F., Yang, Y., and Hao, W.: Antarctic ice-sheet structures retrieved from P-wave coda autocorrelation method and comparisons with two other single-station passive seismic methods, Journal of Glaciology, 66, 153–165, 2020.

Yan, S., Blankenship, D. D., Greenbaum, J. S., Young, D. A., Li, L., Rutishauser, A., Guo, J., Roberts, J. L., van Ommen, T. D., Siegert, M. J., et al.: A newly discovered subglacial lake in East Antarctica likely hosts a valuable sedimentary record of ice and climate change, Geology, 50, 949–953, 2022.

Yang, Z., Hembd, J., Chen, H., and Yang, J.: Reverse time migration of multiples: Applications and challenges, The Leading Edge, 34, 780–786, 2015.

Yilmaz, Ö.: Seismic data analysis, vol. 1, Society of exploration geophysicists Tulsa, 2001.

Zhou, W., Butcher, A., Brisbourne, A. M., Kufner, S.-K., Kendall, J.-M., and Stork, A. L.: Seismic noise interferometry and distributed acoustic sensing (DAS): Inverting for the firn layer S-velocity structure on Rutford Ice Stream, Antarctica, Journal of Geophysical Research: Earth Surface, 127, e2022JF006 917, 2022.